End effector admittance control of parallel manipulators without force sensor

An observer-based control method to improve haptic feedback

Alfons R. Schure

Master of Science Thesis

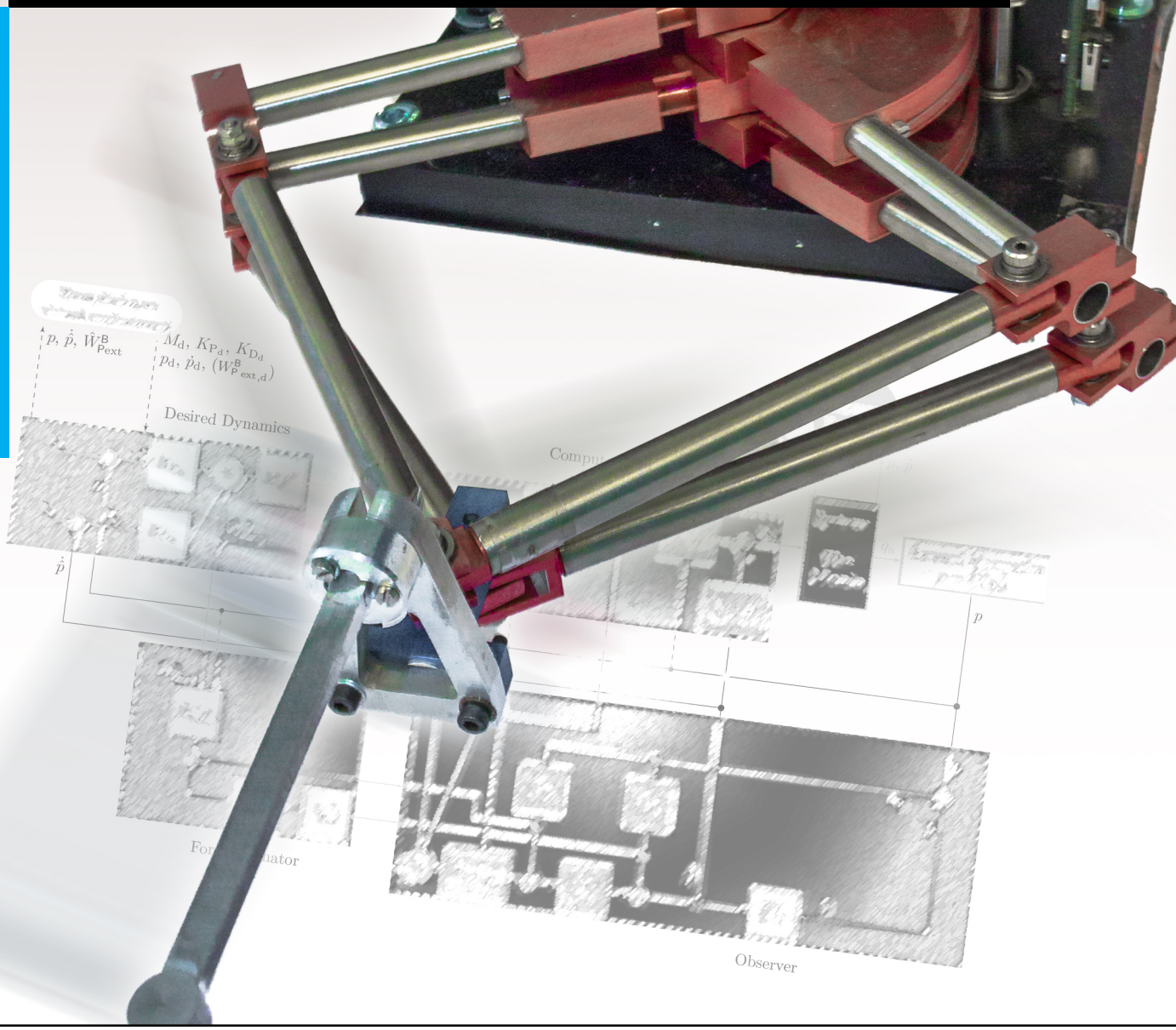

TU Delft Delft University of Technology

Delft Center for Systems and Control

End effector admittance control of parallel manipulators without force sensor

An observer-based control method to improve haptic feedback

Master of Science Thesis

For the degree of Master of Science in Mechanical Engineering at Delft University of Technology

Alfons R. Schure

April 4, 2016

Faculty of Mechanical, Maritime and Materials Engineering (3mE) · Delft University of Technology

The work in this thesis is done in cooperation with the Haptics Lab at Delft University of Technology

Abstract

A telemanipulation system lets a human operator manipulate an environment on distance, using a master and a slave device, which are connected by a bilateral controller that controls the master and the slave device and provides the communication between these devices. The master device is manipulated by the operator and these actions are transferred to the slave device, using the bilateral controller. The interaction forces between the slave device and the remote environment are fed back to the operator, which provides awareness and allows a task to be executed efficiently and safely.

Currently, one of the limitations of telemanipulation systems is that interaction forces are typically indirectly transferred to the human operator. Firstly, a commonly used concept to determine the feedback forces, is by coupling the master and slave position, using a proportional controller. Secondly, feedback forces are generally applied on the master device, which then transfers these forces to the operator through its end effector. Because of the dynamics of the master device, these forces are distorted as they are transferred to the operator. This reduction in force feedback quality decreases awareness of the operator and thereby likely reduces his or her task performance.

To minimize the distortion of the feedback forces by the dynamics of the master device, often a parallel manipulator is used as master device. Compared to a serial manipulator, a parallel manipulator has the advantage that the moving masses are small, because the actuators are positioned at the base. However, the difficulty of parallel manipulators is the kinematic and dynamic modeling of the device, which is much more complex than the modeling of serial manipulators.

The goal of this thesis is to improve force feedback quality. This is achieved through the design of a local admittance controller for a parallel master device, which will cancel out the dynamics of the parallel master device and allows them to be replaced by desired dynamics (desired mass, damping and stiffness). Using this approach, the feedback quality will not only be of higher quality, but will also enable a more complete and intuitive method to design the

force feedback.

However, generally an admittance controller requires the external force applied by the operator as input. Force sensors are expensive and fragile. As a more cost-effective solution, in this thesis the external force will be obtained by force estimation using a model based observer. The model based observer only requires the position measurements, and control wrench (combination of force and torque) at the end effector, as input.

The admittance controller for the parallel master device, without the use of a force sensor, is configured by combining insights from different fields of robot analysis and control. The control algorithm will be build up by a computed torque controller, the desired dynamics to shape desired acceleration, an observer, an observer based force estimator and methods to derive a kinematic and a dynamic model of a parallel manipulator. The control method is tested on a three degrees of freedom planar parallel device: the Munin.

The tests show that the algorithm is able to replace the dynamics of the master device with desired dynamics, such that the device admits a certain motion, with respect to the desired dynamics and the external force applied by the human operator. The limits of the range of desired stiffness, damping and mass, that can be projected on the manipulator's end effector by the control algorithm, are explored. This range is large enough to conclude that **the algorithm is suitable to be used on parallel master devices, to project desired dynamics on the end effector of the device, without the use of a force sensor.**

The control algorithm is designed to control the master device of a telemanipulation system. This enables a intuitive configuration of force feedback. The desired dynamics can be shaped, which can be beneficial to advanced control concepts, such as haptic shared feedback and model mediated control, on top of the feedback directly available form the measurements at the slave device. Furthermore, the control algorithm could also be beneficial for the safe operation for all kinds of devices that cooperate with a human, because of the force estimation, instead of force measurement on one point of the device, will react to all forces applied anywhere on the device.

Table of Contents

Preface

Over a year ago I have read the Msc assignment, proposed by Gabriel Delgado Lopes and Teun Hoevenaars, to work on the control strategies for parallel haptic master devices. Because the control of mechanically complex dynamics is my field of interest, I started working on this research with great motivation. During the work and the struggles to keep focussed on one research question, I enjoyed becoming more familiar with the tools of screw theory, with the possibility to keep the mathematics and the code general so it can be used for many systems. Getting the opportunity to apply this to an admittance controller scheme, which got my attention since I have heard about it in a *Control methods for robotics* lecture, made this thesis subject really fit my interests.

To have the ability to test the control algorithm on a real device, the Munin, and not just in simulation, motivated me a lot and was fun to do. Furthermore, the Munin showed me some errors in the controller, which had to be fixed and did not have shown up in simulation. Two times the Munin tried to point out my mistakes with such an enthusiasm that it even broke its own cables, which took me a couple of hours to repair.

Now the thesis is written and the results are satisfactory, I would like to thank my supervisors Gabriel Delgado Lopes en Teun Hoevenaars for keeping me focussed on just one research goal, with special thanks to Teun, who took a lot of time to guide me throughout the whole process and taught me on screw theory and the writing of a thesis. Also great thanks to all the members of the Haptics lab for showing their interest for my research and help during the discussion we had on the performance of the controller and the possible applications. Thanks to Klaartje for checking my thesis on the use of proper English and thanks to my parents and girlfriend for the kind words and patience during this graduation project.

I hope you enjoy reading.

Alfons Schure

Delft, April 4, 2016.

Chapter 1

Introduction

A telemanipulation system enables a human operator to manipulate an environment from a distance. Telemanipulation is aimed at tasks that need to be executed in an environment unsuitable for direct human presence, and which are too difficult to perform by a fully automated robot. An environment can be unsuitable for human presence due to safety aspects or the size of the task. Examples are maintenance of nuclear plants, robotic arms in space, micro engineering [1][2] and surgery [3].

The total telemanipulation system consists of the human operator, the master device, a bilateral controller containing the control algorithms and communication line, the slave device and the environment of the slave where the task is performed, as shown in figure 1-1 [4]. The master device is manipulated by the operator and these actions are transferred to the slave device, using the bilateral controller. Therefore, a telemanipulation device allows a human operator to manipulate the environment through the slave device, using the master device.

To enable the human operator to perform his task, he will require feedback from the slave device and its environment. A camera and a microphone can give audio [5] and visual feedback through a monitor and a speaker to the operator. In addition to visual and audio feedback, haptic feedback can be given to the operator in order to create a feel of the environment. The concept of haptic feedback includes all the feedback that can be applied to the the touch sense of the operator [6]. Haptic feedback can consist of vibrations from a phone or game controller [7] or more direct force feedback. It allows the human operator of the master device to feel the interaction forces between the remote environment and the end effector of the slave device. Haptic force feedback has been proven to let the operator perform tasks more

Figure 1-1: Telemanipulation system

efficiently, when using a telemanipulation device [6].

A measure for the quality of a telemanipulation device is the transparency of the system. Transparency can be defined as the amount of equality between the master and the slave device in movements and forces [4]. A fully transparent system (transparency = 1) will transmit the feel to the operator, as if he is manipulating the environment directly. Furthermore, the controlled telemanipulation device has to be stable. Stability analysis of the total telemanipulation system with force feedback is not addressed in this thesis, but discussed extensively in general [9] [10], while assuming large time delays in the communication between master and slave [4], and considering the impedance of the human operator [11].

Currently, the force feedback through the end effector of the master device to the human operator is often [8] created by a proportional force, with respect to the relative position and velocity difference between the master and slave end effector (relative difference: both measured in their own reference frame). The proportional force with respect to the position difference can be interpreted as a stiffness, and the proportional force with respect to the velocity difference as damping. Both forces together can be interpreted as a virtual spring and damper between the master and slave end effectors. Because of the dynamics of the master device, the feedback forces are distorted as they are transferred to the operator. This reduction in force feedback quality decreases awareness of the operator and thereby likely reduces his or her task performance.

To minimise the influence of the dynamics of the master device, the moving mass of the master device needs to be small. In order to achieve this, often parallel devices are used as haptic master device. A parallel device consists of multiple serial legs connecting the end effector to the base. This has the advantage that all actuators and sensors can be placed at the base, to reduce the moving mass. (In a device consisting out of a single serial leg, all joints would require an actuator, which results in moving the relative heavy actuators around.) Other advantages of parallel manipulators are the higher force density and better pose measurement compared to serial manipulators (assuming a well designed parallel manipulator). Disadvantages of parallel manipulators compared to serial manipulators are the limited workspace, the mechanical complexity because of the higher number of required joints and the more complex and less straightforward methods that are needed for the system model analysis [12].

The goal of this thesis is to improve the force feedback quality. To let the operator experience only the feedback forces and not the dynamics of the master device, the dynamics of the master device should be compensated by the controller, for which a computed torque control scheme can be used. To improve the quality of the force feedback, more dynamic aspects besides stiffness and damping can be taken into account. The desired dynamics for the force feedback could be derived from the measurements at the slave device. These desired dynamics generally include direct forces plus position, velocity and acceleration based forces: Desired stiffness, desired damping and desired mass with position and velocity references.

Therefore, an admittance controller will be used, which can the replace existing dynamics of the parallel haptic master device by desired dynamics. An admittance controller admits a

certain motion, according to the desired dynamics and the force the human operator applies at the end effector of the master device. This will give the operator the illusion he is moving a system that has the desired dynamics.

An admittance controller needs, besides a model of the system, measurements of the position and velocity of the device and of the external force applied to the end effector by the human operator. Because of economical reasons, often only position measurements at the actuators are available (which can be used to obtain the position of the end effector using the systems forward kinematics). Multi-degree of freedom force sensors are fragile and very expensive.

With only position measurements available, the velocity of the end effector and the external force applied to the end effector can be obtained by estimation. To estimate the present velocity and external force, a model based observer will be used, which requires a accurate model of the parallel haptic master device.

Therefore, the goal is to implement an admittance controller on a parallel haptic master device without the use of an expensive force sensor. This will be achieved by combining computed torque control based admittance control, with the modeling of parallel devices, and the estimation of velocities and forces by use of a model based observer.

The structure of this thesis is as follows. First, the general analysis of a kinematic and dynamic model of a parallel manipulator and the explanation of a model based observer and controller are given in chapter 2. To test the proposed schemes a three degree of freedom planar parallel haptic master device, called the Munin, is used. The mechanical setup for this device is shown in chapter 3. In addition, the general controller, observer and model methods from chapter 2 are adjusted and applied to the test setup. The model analysis of the test setup is shown in chapter 4. The adjusted controller and observer structure is shown and explained in chapter 5. To validate the applied admittance controller, tests are executed and the results from the measurements are shown in chapter 6. Next the results will be discussed in chapter 7. Conclusions on the performance of the proposed admittance controller on a parallel haptic master device, without the use of an expensive force sensor, are given in chapter 8.

The main novelty of the work performed in this thesis is the combination of insights from three fields of robot analysis and control: The admittance controller, the observer based force estimation, and the modeling of parallel manipulators. The use of computed torque controller based admittance control on parallel mechanisms has not been described in literature. Other computed torque controllers applied to parallel mechanisms, often only considers the end effector mass or the legs, instead of all moving masses as done in this thesis. Furthermore, the use of (observer based) force estimation in admittance control is introduced in this thesis.

Additionally, the controller is developed such that it can also be easily adapted for use in more advanced control strategies, such as haptic shared control or model-mediated control. These strategies rely on additional feedback based on virtual stiffness, dampers, and (in the case of model-mediated control) masses.

Chapter 2

Mathematical Background

2-1 Parallel manipulator analysis

2-1-1 Introduction

A parallel device consists of several legs, all connected to both the base and the end effector of the device. Each leg consist out of multiple links and joints connecting those links. The counterpart of a parallel device is a serial device, where one leg is in between the base and the end-effector.

Parallel devices have advantages compared to serial devices for use as a haptic master device. The main advantage is the low inertia of the moving parts, because all actuators can be placed at the non-moving base of the device. A low inertia reduces the feeling of the master device itself, and therefore can improve the feeling of the projected dynamics. Other advantages are the higher accuracy and the higher force density using the same materials [12].

There are also some drawbacks on the use of parallel devices. The workspace is smaller compared to serial devices and there is a relative large amount of joints, which causes a greater complexity in the mechanical design and assemblage. Another disadvantage of parallel devices is the higher complexity in mathematical system modeling. This complexity is caused by the multiple solutions of the end-effector position for the known actuator angles (as shown in figure 2-1), and the dependencies between the legs.

2-1-2 Notations

This section will explain the notations used to describe the geometry and movements of a parallel device and the forces and torques working on that device. This includes the notation

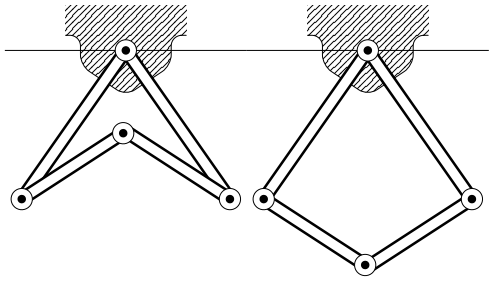

Figure 2-1: Multiple end effector position are possible for the same measured actuated (base) angles

for local coordinate systems and the points in that coordinate system and the notation of velocities, forces and torques using screw theory [13].

A parallel device consist of multiple legs that consist of links connected by joints, where $\mathsf{L}_{r,s}$ is the s^{th} link of leg r and $\mathsf{J}_{r,t}$ is the t^{th} joint of leg r. For better readability, the subscripts r, t and s will not be written when trivial. Therefore $\mathsf{J} = \mathsf{J}_{r,t}$ and $\mathsf{L} = \mathsf{L}_{r,s}$.

Coordinate systems

To describe the relations between different points of the parallel manipulator coordinate systems are placed at all relevant points. A joint has two coordinate systems. One at the base side of its motion, named $\Psi_{\mathsf{J}_{r,t}}$ and one at the end effector side of the joints motion named $\Psi_{\mathsf{L}_{r,t}}$. Each link has three coordinate systems, of which two are shared with respectively the joint at the base side and the end effector side of the link. The coordinate system at the base side of the link is $\Psi_{\mathsf{L}_{r,s}}$ and the coordinate system at the end effector side of the link is $\Psi_{\mathsf{J}_{r,s+1}}$. The third coordinate system located at each link is placed at the center of mass of the link and named $\Psi_{\mathsf{M}_{r,s}}$.
Three additional coordinate systems will be added to the system: One attached to the base, named Ψ_{B}, one attached to the end effector named Ψ_{E} and another one at the end effector location, but rotated parallel to the base: Ψ_{P}.

Position of points

A point with index u in coordinate system Ψ_l is described as

$$\alpha_u^l = \begin{bmatrix} x & y & z & 1 \end{bmatrix}^\top, \tag{2-1}$$

the vector notation convention as in [13]. To describe this point in coordinate system m a homogeneous transformation matrix H_l^m is used.

$$\alpha_u^m = H_l^m \cdot \alpha_u^l. \tag{2-2}$$

For example let

$$\alpha_u^{\mathsf{J}} = \begin{bmatrix} 0 & 0 & 0 & 1 \end{bmatrix}^\top, \tag{2-3}$$

be a point α_u in (the origin of) Ψ_{J}, then

$$\alpha_u^{\mathsf{L}} = H_{\mathsf{J}}^{\mathsf{L}} \cdot \alpha_u^{\mathsf{J}} \tag{2-4}$$

is that same point expressed in coordinate system Ψ_{L}. With $s+1=t$ (note: $\mathsf{J} = \mathsf{J}_{r,t}$ and $\mathsf{L} = \mathsf{L}_{r,s}$) and the length of L being 0.123m this becomes:

$$\alpha_u^{\mathsf{L}} = H_{\mathsf{J}}^{\mathsf{L}} \cdot \alpha_u^{\mathsf{J}} = \begin{bmatrix} 1 & 0 & 0 & 0.123 \\ 0 & 1 & 0 & 0 \\ 0 & 0 & 1 & 0 \\ 0 & 0 & 0 & 1 \end{bmatrix} \begin{bmatrix} 0 \\ 0 \\ 0 \\ 1 \end{bmatrix} = \begin{bmatrix} 0.123 \\ 0 \\ 0 \\ 1 \end{bmatrix}. \tag{2-5}$$

Having all homogeneous matrices between the coordinate systems next to each other, all the other homogeneous matrices between coordinate systems can be found by multiplying the matrices:

$$H_l^k = H_m^k \cdot H_l^m. \tag{2-6}$$

Transformations in the other direction are found by inverting the homogeneous matrix:

$$\left(H_n^k\right)^{-1} = \begin{bmatrix} {R_n^k}^\top & -{R_n^k}^\top \cdot a_n^k \\ 0 & 1 \end{bmatrix} = H_k^n, \tag{2-7}$$

for

$$H_n^k = \begin{bmatrix} R_n^k & a_n^k \\ 0 & 1 \end{bmatrix}. \tag{2-8}$$

Often a point in the origin of a coordinate system will be used. A point in the origin of coordinate system Ψ_l described in coordinate system Ψ_m will be written as o_l^m. Therefore α_u^{L} in the example in equation 2-5, which is located in the origin of Ψ_{J} can be written as $o_{\mathsf{J}}^{\mathsf{L}}$.

Twists

The combination of the translational and rotational velocity between certain bodies will be described by a twist. In the notation the twist will be described between the coordinate systems attached to those bodies. The motion of Ψ_l with respect to Ψ_m expressed in Ψ_k will be written as the twist $T_l^{k,m}$. A twist is a column vector with six entries; three in ω and three in v, and can be interpretted as follows (Mozzi theorem):

$$T_l^{k,m} = \begin{bmatrix} \omega \\ v \end{bmatrix} = \underbrace{\begin{bmatrix} \omega \\ r \times \omega \end{bmatrix}}_{\text{rotation}} + \lambda \cdot \underbrace{\begin{bmatrix} 0 \\ \omega \end{bmatrix}}_{\text{translation}}, \tag{2-9}$$

where r is perpendicular to ω and goes from the origin to ω. The crossproduct $r \times \omega$ is the velocity component along ω and $\lambda \cdot \omega$ the one orthogonal to ω.

Twists can be described in a different coordinate system by the adjoint of the homogeneous matrix between the coordinate systems:

$$T_l^{k,m} = Ad_{H_n^k} T_l^{n,m}, \tag{2-10}$$

where

$$Ad_{H_n^k} = \begin{bmatrix} R_n^k & 0 \\ \tilde{a}_n^k R_n^k & R_n^k \end{bmatrix},$$

for H_n^k as in equation 2-8, and

$$a = \begin{bmatrix} a_1 \\ a_2 \\ a_3 \end{bmatrix} \Rightarrow \tilde{a} = \begin{bmatrix} 0 & -a_3 & a_2 \\ a_3 & 0 & -a_1 \\ -a_2 & a_1 & 0 \end{bmatrix}.$$

Homogeneous transformation matrices for joints

Besides the static homogeneous matrices, such as the one shown equation 2-5 also the transformations in the joints are defined by the homogeneous matrices between the coordinate systems. These homogeneous matrices are built up using the unit twist of their joint and the joint coordinate $q = q_{r,t}$ of $\mathsf{J} = \mathsf{J}_{r,t}$. (For example: If it is a rotational joint, q is an angle.)

$$H_{\mathsf{J}}^{\mathsf{L}}(q) = e^{\hat{T}_{\mathsf{L}}^{\mathsf{J},\mathsf{J}} \cdot q} \cdot H_{\mathsf{J}}^{\mathsf{L}}(0), \tag{2-11}$$

(note: $e^{\hat{T}_{\mathsf{L}}^{\mathsf{J},\mathsf{J}} \cdot q}$ will be solved analytically with use of the Rodriguez formula).

For example the unit twist of J with respect to L in coordinate system Ψ_{J} of a rotation q around the z-axis is

$$\hat{T}_{\mathsf{L}}^{\mathsf{J},\mathsf{J}} = \begin{bmatrix} 0 & 0 & 1 & 0 & 0 & 0 \end{bmatrix}^\top, \tag{2-12}$$

and with

$$H_{\mathsf{L}}^{\mathsf{J}}(0) = \begin{bmatrix} 1 & 0 & 0 & 0 \\ 0 & 1 & 0 & 0 \\ 0 & 0 & 1 & 0 \\ 0 & 0 & 0 & 1 \end{bmatrix}, \tag{2-13}$$

then:

$$H_{\mathsf{L}}^{\mathsf{J}}(q) = \begin{bmatrix} \cos q & -\sin q & 0 & 0 \\ \sin q & \cos q & 0 & 0 \\ 0 & 0 & 1 & 0 \\ 0 & 0 & 0 & 1 \end{bmatrix}. \tag{2-14}$$

To express a unit twist in another coordinate system the same transformation as for twists can be used, as is shown in equation 2-10.

Wrenches

A method to write the forces and torques applied in a coordinate system on a body is by using a wrench. A wrench is a co-vector (expressed as a row vector) with six entries, where the first three represent the torques and the next three terms represent the linear force ($W_l^m = \begin{bmatrix}\tau & F\end{bmatrix}$) such that the wrench between two bodies (described as a wrench between the coordinate systems) multiplied by the twist between the same two bodies is the power applied by the wrench: Power $= W_l^m T_l^{k,m}$. The wrench can be interpreted as follows (Poinsot theorem):

$$\begin{bmatrix}\tau \\ F\end{bmatrix}^\top = \underbrace{\begin{bmatrix}r \times F \\ F\end{bmatrix}^\top}_{\text{force along screw axis F}} + \lambda \cdot \underbrace{\begin{bmatrix}F \\ 0\end{bmatrix}^\top}_{\text{moment around screw axis F}} . \tag{2-15}$$

A transposed wrench can be transformed to another coordinate system using the transposed adjoint of the inverse homogeneous matrix, when compared to a coordinate transformation of a twist:

$$(W_l^m)^\top = Ad_{H_m^k}^\top \cdot (W_l^k)^\top. \tag{2-16}$$

2-1-3 Kinematics

In this section the general analysis of the kinematic maps between positions and velocities of all defined coordinate systems in a parallel manipulator is shown. The initial configuration of the parallel system is assumed to be known, which is not trivial, because often multiple configurations are possible when the passive joint coordinates are not measured.

Inverse Kinematics

The inverse kinematics G of a manipulator describe the joint coordinates q or actuated / measured joint coordinates q_a (which are angles in the case of rotational joints) as a function of the end effector (workspace / task space) coordinates p.

$$q = G(p) \quad \| \quad q_\mathrm{a} = G_a(p). \tag{2-17}$$

The analysis for a parallel manipulator will be done for each leg separately. For a known configuration (it is known in what range the joint coordinates are) the function can be built up using the standard goniometric tools, such as the sine and cosine rules.

The alternative is to use the joint coordinate dependent homogeneous transformation matrix to express the position of the origin of the coordinate system placed at the end effector in the coordinate system located at the base of the device. Solving this expression for the known end effector position will generally lead to multiple solutions, because multiple configurations are possible. The right configuration can be picked when the configuration is known, but in general this method is more computational complex than the goniometric method.

Forward Kinematics

The forward kinematics D describe the end effector position p as a function of (the actuated / measured) joint coordinates q_{a}.

$$p = D(q_{\mathrm{a}}). \tag{2-18}$$

The forward kinematics of a parallel manipulator can be found using the homogeneous matrices to describe the end effector position in Ψ_{B} as function of all joint coordinates. This can be done because the end effector position is equal for all legs. Generally the resulting equation from this equality is very complex and contains many variables. Therefore this is difficult to solve analytically. For simple parallel manipulators the goniometric tools can be used to obtain the forward kinematics function, which is done for the test setup in this thesis. Often the determination of the end effector position will be the fastest using a iterative process, for example the Newton-Raphson method, using the inverse kinematics function and the Jacobian (introduced in next subsection) [12]:

$$p_{k+1} = p_k + J\left(q_{\mathrm{a}} - G\left(p_k\right)\right). \tag{2-19}$$

In order to converge to the right solution $p = p_k$ of end effector coordinates, equation 2-19 will be repeated until $\left\|q_{\mathrm{a}} - G_a(p_k)\right\| < \epsilon$ for a fixed threshold ϵ.

Inverse Jacobian

The inverse Jacobian matrix maps the end effector twist (in base coordinates) $T_{\mathsf{E}}^{\mathsf{B},\mathsf{B}}$ to the joint velocities.

$$\dot{q} = J^{-1} \cdot T_{\mathsf{E}}^{\mathsf{B},\mathsf{B}}. \tag{2-20}$$

The inverse Jacobian will be determined for all separate joints, building the inverse Jacobian row by row (equation 2-21) [14][15][16]:

$$\dot{q} = \begin{bmatrix} J_1^{-1} \\ J_2^{-1} \\ \vdots \\ J_i^{-1} \end{bmatrix} \cdot T_{\mathsf{E}}^{\mathsf{B},\mathsf{B}}. \tag{2-21}$$

For the analysis the manipulator arm in figure 2-2 is used as example. This one manipulator leg is leg r. Taking the forward Jacobian, that can be constructed from the unit twists $\hat{T}_{\mathsf{L}_{r,t}}^{\mathsf{B},\mathsf{J}_{r,t}}$ of the joints (equation 2-22), and multiplying this with a wrench W_t^{B} reciprocal to all joint twists but one (equation 2-23), will leave one of the terms. This is because a twist multiplied

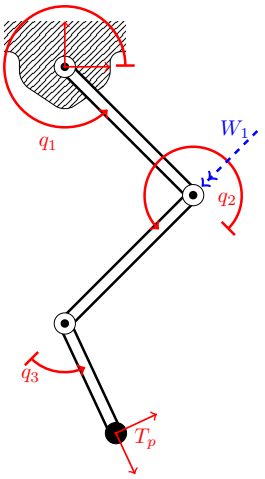

Figure 2-2: Serial manipulator arm

by a wrench reciprocal to that twist is zero (equation 2-24 and 2-25). That will result in an equation describing the relation between the end-effector twist $T_{\mathsf{E}}^{\mathsf{B},\mathsf{B}}$ and one of the joint velocities (equation 2-26 and 2-27).

$$T_{\mathsf{E}}^{\mathsf{B},\mathsf{B}} = \begin{bmatrix} \hat{T}_{\mathsf{L}_{r,1}}^{\mathsf{B},\mathsf{J}_{r,1}} & \hat{T}_{\mathsf{L}_{r,2}}^{\mathsf{B},\mathsf{J}_{r,2}} & \hat{T}_{\mathsf{L}_{r,3}}^{\mathsf{B},\mathsf{J}_{r,3}} \end{bmatrix} \cdot \begin{bmatrix} \dot{q}_{r,1} & \dot{q}_{r,2} & \dot{q}_{r,3} \end{bmatrix}^T, \tag{2-22}$$

$$W_{1,1}^{\mathsf{B}} \cdot T_{\mathsf{E}}^{\mathsf{B},\mathsf{B}} = \begin{bmatrix} W_{1,1}^{\mathsf{B}} \hat{T}_{\mathsf{L}_{r,1}}^{\mathsf{B},\mathsf{J}_{r,1}} & W_{1,1}^{\mathsf{B}} \hat{T}_{\mathsf{L}_{r,2}}^{\mathsf{B},\mathsf{J}_{r,2}} & W_{1,1}^{\mathsf{B}} \hat{T}_{\mathsf{L}_{r,3}}^{\mathsf{B},\mathsf{J}_{r,3}} \end{bmatrix} \cdot \begin{bmatrix} \dot{q}_{r,1} & \dot{q}_{r,2} & \dot{q}_{r,3} \end{bmatrix}^T, \tag{2-23}$$

$$W_{1,1}^{\mathsf{B}} \cdot T_{\mathsf{E}}^{\mathsf{B},\mathsf{B}} = \begin{bmatrix} W_{1,1}^{\mathsf{B}} \hat{T}_{\mathsf{L}_{r,1}}^{\mathsf{B},\mathsf{J}_{r,1}} & 0 & 0 \end{bmatrix} \cdot \begin{bmatrix} \dot{q}_{r,1} & \dot{q}_{r,2} & \dot{q}_{r,3} \end{bmatrix}^T, \tag{2-24}$$

$$W_{1,1}^{\mathsf{B}} \cdot T_{\mathsf{E}}^{\mathsf{B},\mathsf{B}} = W_{1,1}^{\mathsf{B}} \cdot \hat{T}_{\mathsf{L}_{r,1}}^{\mathsf{B},\mathsf{J}_{r,1}} \cdot \dot{q}_{r,1}, \tag{2-25}$$

$$\Rightarrow \underbrace{\left(\left(W_{1,1}^{\mathsf{B}} \cdot \hat{T}_{\mathsf{L}_{r,1}}^{\mathsf{B},\mathsf{J}_{r,1}} \right)^{-1} \cdot W_{1,1}^{\mathsf{B}} \right)}_{J^{-1}} \cdot T_{\mathsf{E}}^{\mathsf{B},\mathsf{B}} = \dot{q}_{r,1}, \tag{2-26}$$

$$\Rightarrow \dot{q}_{r,1} = J^{-1} \cdot T_{\mathsf{E}}^{\mathsf{B},\mathsf{B}}, \tag{2-27}$$

(note: $\left(W_{r,t}^{\mathsf{B}} \cdot \hat{T}_{\mathsf{L}_{r,t}}^{\mathsf{B},\mathsf{J}_{r,t}} \right)$ is a scalar and therefore the inverse is determined straightforward).

Repeating those steps for all joints in the parallel manipulator will result in a full inverse Jacobian of the system (equation 2-21). Depending on the goal of the Jacobian the choice can be made to only consider the actuated joints or the joints of one of the legs in the parallel manipulator.

Forward Jacobian

The forward Jacobian is undetermined assuming only knowledge about the four angles at the base, because multiple configurations of the system are possible for the measured joint angles. The forward Jacobian can be created by taking the (pseudo) inverse of the in this section

created inverse Jacobian matrix:

$$J = \left(J^{-1}\right)^{-1}. \tag{2-28}$$

2-1-4 Dynamics

The direct dynamics of a manipulator yields the acceleration as a function of the internal and external forces and torques. The inverse dynamics yields the required torque for a given acceleration and internal force. A typical notation for the inverse dynamics in workspace coordinates p is shown in equation 2-29:

$$W^{\mathsf{B}}_{\mathsf{P}\,\mathrm{c}} = M(p)\cdot\ddot{p} + C(p,\dot{p}) + K(p) - W^{\mathsf{B}}_{\mathsf{P}\,\mathrm{ext}}. \tag{2-29}$$

The $p = \begin{bmatrix} p_x & p_y & p_z & p_{\theta_x} & p_{\theta_y} & p_{\theta_z} \end{bmatrix}^\top$ contains the position $\begin{bmatrix} p_x & p_y & p_z \end{bmatrix}^\top$ expressed in Ψ_{B} and the angles $\begin{bmatrix} p_{\theta_x} & p_{\theta_y} & p_{\theta_z} \end{bmatrix}^\top$ in Ψ_{P}. $W^{\mathsf{B}}_{\mathsf{P}\,\mathrm{c}}$ is the control wrench projected on the end effector (control torques $\tau_{q_\mathrm{a}} = J^\top \cdot W^{\mathsf{B}}_{\mathsf{P}\,\mathrm{c}}$), $W^{\mathsf{B}}_{\mathsf{P}\,\mathrm{ext}}$ is the external wrench applied to the end effector, $M(p)$ is the mass matrix in Ψ_{P}, $C(p,\dot{p})$ contains all velocity dependent wrenches including Coriolis effects and friction forces and $K(p)$ includes the position dependable effects such as gravity and stiffness.

The direct dynamics can be found from equation 2-29 by inverting the mass matrix $M(p)$:

$$\ddot{p} = M^{-1}(p)\cdot\left(-C(p,\dot{p}) - K(p) + W^{\mathsf{B}}_{\mathsf{P}\,\mathrm{ext}} + W^{\mathsf{B}}_{\mathsf{P}\,\mathrm{c}}\right). \tag{2-30}$$

Because all motion and force is expressed in workspace coordinates Ψ_{P} also the inertial, coriolis and other forces need to be projected on Ψ_{P}. Identification methods do exist [17], but in this thesis the system model will be determined analytically. The used analytical method is the Euler-Lagrange method [13][18]. Another often used method for parallel manipulators is the use of virtual work [19][20].

Mass matrix

All masses can be projected on Ψ_{P}, to create a mass matrix located in Ψ_{P} that depends on p. The total mass is a summation of all projected masses, including all links s and joints t of all legs r.

$$M(p) = \sum_r \left(\sum_s \left(M(p)_{\mathsf{L}_{r,s}}\right) + \sum_t \left(M(p)_{\mathsf{J}_{r,t}}\right) \right), \tag{2-31}$$

in which the projection of the mass and inertia on Ψ_{P} of one link $\mathsf{L} = \mathsf{L}_{r,s}$ is determined by:

$$M(p)_{\mathsf{L}} = Ad^\top_{H^{\mathsf{B}}_{\mathsf{P}}} \cdot J_r^{-\top} \cdot J_{\mathsf{L}}^\top \cdot Ad^\top_{H^{\mathsf{L}}_{\mathsf{B}}} \cdot \mathcal{I}_{\mathsf{L}} \cdot Ad_{H^{\mathsf{L}}_{\mathsf{B}}} \cdot J_{\mathsf{L}} \cdot J_r^{-1} \cdot Ad_{H^{\mathsf{B}}_{\mathsf{P}}}, \tag{2-32}$$

for

$$\mathcal{I}_{\mathsf{L}} = \begin{bmatrix} \begin{bmatrix} I_{\mathsf{L},xx} & I_{\mathsf{L},xy} & I_{\mathsf{L},xz} \\ I_{\mathsf{L},yx} & I_{\mathsf{L},yy} & I_{\mathsf{L},yz} \\ I_{\mathsf{L},zx} & I_{\mathsf{L},zy} & I_{\mathsf{L},zz} \end{bmatrix} & \mathbf{0} \\ \mathbf{0} & m \cdot \begin{bmatrix} 1 & 0 & 0 \\ 0 & 1 & 0 \\ 0 & 0 & 1 \end{bmatrix} \end{bmatrix}, \tag{2-33}$$

, with mass m and inertia I.
$J_{\mathsf{L}} = J_{\mathsf{L}_{r,s}}$ in equation 2-32 is the Jacobian matrix, that will map the joint velocities $1 \cdots s$ of leg r to the twist of L, with respect to the base and expressed in base coordinates Ψ_{B}:

$$T^{\mathsf{B},\mathsf{B}}_{\mathsf{L}_{r,s}} = J_{\mathsf{L}_{r,s}} \dot{q}_r. \tag{2-34}$$

This Jacobian J_{L} can be built up using the unit twists of the joints between Ψ_{L} and Ψ_{B} and zeros to fill up the matrix to a $6 \times n$ matrix, where n is the total amount of joints in leg r:

$$J_{\mathsf{L}_{r,s}} = \begin{bmatrix} \hat{T}^{\mathsf{B},\mathsf{J}_{r,1}}_{\mathsf{L}_{r,1}} & \hat{T}^{\mathsf{B},\mathsf{J}_{r,2}}_{\mathsf{L}_{r,2}} & \cdots & \hat{T}^{\mathsf{B},\mathsf{J}_{r,s}}_{\mathsf{L}_{r,s}} & 0 & \cdots & 0 \end{bmatrix}. \tag{2-35}$$

J_r in equation 2-32 is the Jacobian matrix, which maps the joint velocities of leg r to the end effector twist with respect to the base expressed in Ψ_{P}:

$$T^{\mathsf{B},\mathsf{B}}_{\mathsf{P}} = J_r \dot{q}_r. \tag{2-36}$$

The Jacobian J_r^{-1} can be determined by use of the method presented in equation 2-26.

Equation 2-32 is based on the projection of the masses and inertias on the joint coordinates, as shown in [13].

Euler-Lagrange method

To obtain the total dynamics description (equation 2-29), several methods are available. In this thesis the Euler-Lagrange method will be used. For this method we define $\mathcal{L}(p, \dot{p})$ as follows:

$$\mathcal{L}(p, \dot{p}) = \mathcal{T}^*(p, \dot{p}) - \mathcal{V}(p), \tag{2-37}$$

where $\mathcal{V}(p)$ is the potential energy. This potential energy consist of energy stored in deflection of springs and energy stored in height of the mass (mass as descibed in equation 2-31). $\mathcal{T}^*(p, \dot{p})$ is the kinetic co-energy, that will require the mass and the end effector velocity:

$$\mathcal{T}^*(p, \dot{p}) = \frac{1}{2} \dot{p}^\top M(p) \dot{p}. \tag{2-38}$$

Now $\mathcal{L}(p, \dot{p})$ can be used to obtain equation 2-29 by solving the Euler-Lagrange equation, which can be a computational challenge to solve analytically, because of the complex build up of the mass and Jacobian matrices:

$$W^{\mathsf{B}}_{\mathsf{P}} = \frac{d}{dt} \left(\frac{\partial \mathcal{L}(p, \dot{p})}{\partial \dot{p}} \right) - \frac{\partial \mathcal{L}(p, \dot{p})}{\partial p}. \tag{2-39}$$

2-2 Control system

To compensate for the dynamics of the parallel haptic master device, the controller uses a computed torque controller scheme, applied in workspace coordinates. In this section this computed torque controller scheme is explained in text, block schemes and mathematics. The controller assumes full state information, which is available because of the use of an observer (section 2-2-2), including all positions, velocities and external forces. The input of the computed torque controller is a desired acceleration, that can be shaped to act as chosen desired dynamics to create a controller that admits motion for a known external force and/or to project an desired end effector force.

2-2-1 Computed Torque Admittance Controller

A computed torque controller compensates for the dynamics of the parallel haptic master device [21][22]. This control torque is computed by the inverse dynamics in workspace coordinates Ψ_{P}, which was shown in equation 2-29 and repeated here (equation 2-40) with the control wrench $W^{\mathsf{B}}_{\mathsf{P}\,\mathrm{c}}$ mapped to the control torques τ_{q_a} by $\tilde{J}^{\top}(p)$(model of $J^{\top}$), with $\ddot{p}_\mathrm{d}$ representing the desired acceleration. (Note: All models are represented with a tilde [˜] and all observer estimates will have a hat [ˆ].)

$$\tau_{q_\mathrm{a}} = \tilde{J}^{\top}(p)\left(\tilde{M}(p)\cdot\ddot{p}_\mathrm{d} + \tilde{C}(p,\dot{\hat{p}}) + \tilde{K}(p) - \hat{W}^{\mathsf{B}}_{\mathsf{P}\mathrm{ext}}\right), \tag{2-40}$$

in which $\tilde{M}(p)$, $\tilde{C}(p,\dot{\hat{p}})$ and $\tilde{K}(p)$ are the modelled versions of the real $M(p)$, $C(p,\dot{p})$ and $K(p)$ and $\hat{W}^{\mathsf{B}}_{\mathsf{P}\mathrm{ext}}$ is the measured or estimated $W^{\mathsf{B}}_{\mathsf{P}\,\mathrm{ext}}$. When the desired acceleration is zero, the device is infinitely stiff with respect to the external wrench $W^{\mathsf{B}}_{\mathsf{P}\,\mathrm{ext}}$ (assuming perfectly modelled $\tilde{M}(p) = M(p)$, $\tilde{C}(p,\dot{\hat{p}}) = C(p,\dot{p})$ and $\tilde{K}(p) = K(p)$, perfectly measured $\hat{W}^{\mathsf{B}}_{\mathsf{P}\mathrm{ext}} = W^{\mathsf{B}}_{\mathsf{P}\,\mathrm{ext}}$ and an infinitely fast controller).

The shape of the desired acceleration $\ddot{p}_\mathrm{d}$ is often created by a PD (proportional + derivative) controller on the position, or a PI (proportional + integral) controller on the force, or a combination of both force and position control [8][23][24][25][26][27]. In those applications the applied external wrench is not included ($\hat{W}^{\mathsf{B}}_{\mathsf{P}\mathrm{ext}}$ is left out in equation 2-40), which means that the response of the end effector to the external wrench is not linearised.

To let the device act as a linear mass moving in free space, the term $\hat{W}^{\mathsf{B}}_{\mathsf{P}\mathrm{ext}}$ will be considered in equation 2-40 and the acceleration will be shaped to let the device react as a linear desired mass M_d:

$$\ddot{p}_\mathrm{d} = M_\mathrm{d}^{-1}\cdot\hat{W}^{\mathsf{B}}_{\mathsf{P}\mathrm{ext}}. \tag{2-41}$$

Stiffness and damping can be added to this desired acceleration. $K_{\mathrm{P_d}}$ and $K_{\mathrm{D_d}}$, representing a desired stiffness and damping with respect to a desired reference position and twist, can be added to the desired acceleration $\ddot{p}_\mathrm{d}$. Those values will be multiplied by respectively the position error $e_p = p_\mathrm{d} - p$ and twist error $\dot{e}_p = \dot{p}_\mathrm{d} - \dot{p}$ to create a force. If this force is

multiplied by the inverse desired mass M_{d}^{-1}, the $K_{\mathrm{P_d}}$ and $K_{\mathrm{D_d}}$ represent the stiffness and damping in the intuitive units $\frac{\mathrm{N}}{\mathrm{m}}$ and $\frac{\mathrm{N{\cdot}s}}{\mathrm{m}}$ for translations and $\frac{\mathrm{N{\cdot}m}}{\mathrm{rad}}$ and $\frac{\mathrm{N{\cdot}m{\cdot}s}}{\mathrm{rad}}$ for rotations.

$$\ddot{p}_{\mathrm{d}} = M_{\mathrm{d}}^{-1} \cdot \left(\hat{W}^{\mathsf{B}}_{\mathsf{Pext}} + K_{\mathrm{P_d}} \cdot e_p + K_{\mathrm{D_d}} \cdot \dot{e}_p \right). \tag{2-42}$$

When the control torque from equation 2-40 with the desired acceleration from equation 2-42 is applied to the system with the equations of motion shown in equation 2-30, the system will act according to the desired dynamics. This principle is shown in the equation below. (Note: the red part will be replaced in the next step, and the other colors will cancel out in the next step.)

$$\begin{aligned}
\ddot{p} &= M^{-1}(p) \cdot \left(-C(p,\dot{p}) - K(p) + W^{\mathsf{B}}_{\mathsf{P}\,\mathrm{ext}} + W^{\mathsf{B}}_{\mathsf{P}\,\mathrm{c}} \right), && \text{(2-43)} \\
&= M^{-1}(p) \cdot \left(-C(p,\dot{p}) - K(p) + W^{\mathsf{B}}_{\mathsf{P}\,\mathrm{ext}} + J^{-\top} \cdot \tau_{q_{\mathrm{a}}} \right), && \text{(2-44)} \\
&= M^{-1}(p) \cdot \Big(-C(p,\dot{p}) - K(p) + W^{\mathsf{B}}_{\mathsf{P}\,\mathrm{ext}} + \cdots \\
&\quad \cdots + J^{-\top} \cdot \tilde{J}^{\top}(p) \left(\tilde{M}(p) \cdot \ddot{p}_{\mathrm{d}} + \tilde{C}(p,\hat{\dot{p}}) + \tilde{K}(p) - \hat{W}^{\mathsf{B}}_{\mathsf{Pext}} \right) \Big), && \text{(2-45)} \\
&= M^{-1}(p) \cdot \Big(-C(p,\dot{p}) - K(p) + W^{\mathsf{B}}_{\mathsf{P}\,\mathrm{ext}} + \cdots \\
&\quad \cdots + \tilde{M}(p) \cdot M_{\mathrm{d}}^{-1} \cdot \left(\hat{W}^{\mathsf{B}}_{\mathsf{Pext}} + K_{\mathrm{P_d}} \cdot e_p + K_{\mathrm{D_d}} \cdot \dot{e}_p \right) + \cdots \\
&\quad \cdots + \tilde{C}(p,\hat{\dot{p}}) + \tilde{K}(p) - \hat{W}^{\mathsf{B}}_{\mathsf{Pext}} \Big), && \text{(2-46)} \\
&= M^{-1}(p) \cdot \left(\tilde{M}(p) \cdot M_{\mathrm{d}}^{-1} \cdot \left(\hat{W}^{\mathsf{B}}_{\mathsf{Pext}} + K_{\mathrm{P_d}} \cdot e_p + K_{\mathrm{D_d}} \cdot \dot{e}_p \right) \right), && \text{(2-47)} \\
&= M_{\mathrm{d}}^{-1} \cdot \left(\hat{W}^{\mathsf{B}}_{\mathsf{Pext}} + K_{\mathrm{P_d}} \cdot e_p + K_{\mathrm{D_d}} \cdot \dot{e}_p \right), && \text{(2-48)} \\
\Rightarrow\ & \ddot{p} = \ddot{p}_{\mathrm{d}}. && \text{(2-49)}
\end{aligned}$$

This control algorithm is also shown as a block diagram in figure 2-3.

This type of admittance control shapes the desired acceleration, while correcting for the dynamics of the device. Often admittance controllers applied to haptic master devices make use of a simulated model of the desired dynamics, that will react to the measured external wrench or force. In those cases the device itself is controlled to the position of this simulated model by stiff (high gain) position control [28][29][30].

2-2-2 Observer: Estimate end effector Twist and external Wrench

The controller requires the present position and velocity of the system and the external force from the operator to compute the control action. If only position measurements are available, the velocity and external force can be obtained using an observer.

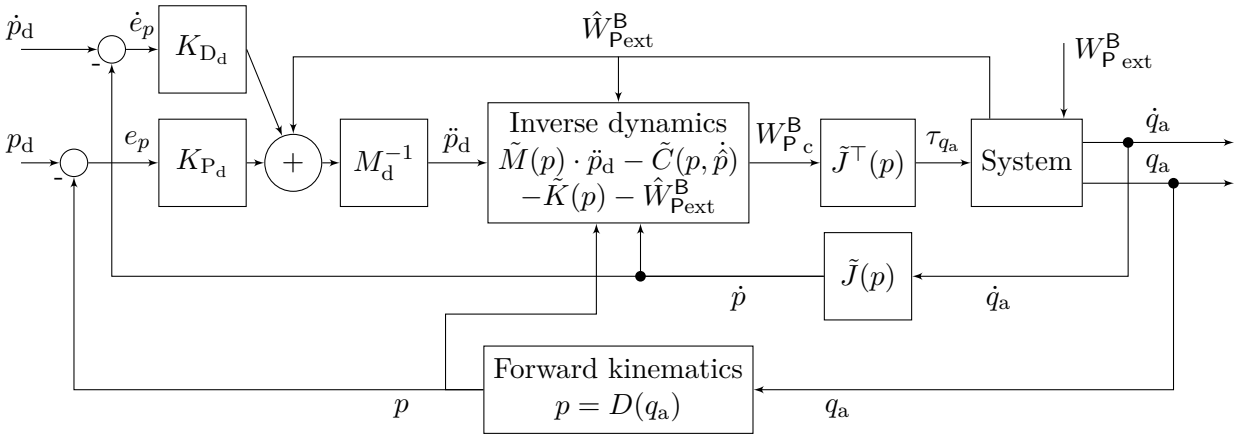

Figure 2-3: Computed torque admittance controller

Velocity observer

The observer consist of a model of the real system containing all model dynamics in workspace coordinates, as shown in equation 2-30. From the model variables the present acceleration is obtained, which leads to the velocity and position after integration. The observer velocity and if required also the observer position can be used in the control algorithm described in section 2-2-1.

Because of disturbances, numerical precision, model errors, and unknown external forces, the observer position $\hat{p}$ will differ from the real position p if not corrected. Therefore the acceleration and velocity of the observer are corrected by an observer gain $L = \begin{bmatrix} L_{\dot{p}} & L_{\ddot{p}} \end{bmatrix}^\top$ multiplied by the error $e_{\hat{p}}$ between the observer position $\hat{p}$ and the real position p, which is obtained from the forward kinematic model and the measurements ($e_{\hat{p}} = p - \hat{p}$):

$$\ddot{\hat{p}}(t) = \tilde{M}^{-1}(p)\cdot\left(-\tilde{C}(p,\dot{\hat{p}}) - \tilde{K}(p) + W^{\mathsf{B}}_{\mathsf{P}\,\mathrm{c}}\right) - L_{\ddot{p}}\cdot e_{\hat{p}}, \tag{2-50}$$

$$\dot{\hat{p}}(t) = \dot{\hat{p}}(0) + \int_0^t \ddot{\hat{p}}(t)\ \mathrm{d}t - L_{\dot{p}}\cdot e_{\hat{p}}, \tag{2-51}$$

$$\hat{p}(t) = \hat{p}(0) + \int_0^t \dot{\hat{p}}(t)\ \mathrm{d}t. \tag{2-52}$$

The observer error $e_{\hat{p}}$ will also be used to estimate the external force $\hat{W}^{\mathsf{B}}_{\mathsf{Pext}}$ the human operator applies to the end effector. Assuming the model is perfect perfect, the observer error will be a result of only $W^{\mathsf{B}}_{\mathsf{P}\,\mathrm{ext}}$. Therefore the effort of the observer gain will be equal to the effort of the external force that is applied by the human operator.

A method to estimate the external force for a linear one degree of freedom system is described in [31]. If the observer is as shown in equation 2-50 and 2-51, but without $\tilde{C}(p,\dot{\hat{p}})$ and $\tilde{K}(p)$, the external force or wrench $W^{\mathsf{B}}_{\mathsf{P}\,\mathrm{ext}}$ results from analysis of the error dynamics:

$$\hat{W}^{\mathsf{B}}_{\mathsf{Pext}}(e_{\hat{p}}) = \tilde{M}(p) \cdot \left(L_{\ddot{p}} \cdot e_{\hat{p}} + L_{\dot{p}} \cdot \dot{e}_{\hat{p}} + \ddot{e}_{\hat{p}} \right). \tag{2-53}$$

For a static force only the $L_{\ddot{p}} \cdot e_{\hat{p}}$ needs to be considered. For non-static forces the term $L_{\dot{p}} \cdot \dot{e}_{\hat{p}}$ can be added and eventually $\ddot{e}_{\hat{p}}$, with the drawbacks of having to find the derivative of the non-smooth observer error $e_{\hat{p}}$. An extension to this force estimation method is described in [32]. It is shown that a second observer can be added, which will also use the estimated external force as input, to determine the force estimation error and correct the value of the estimated external force that will be used in the controller.

If the observer gain L is small, the resulting observer velocity $\dot{\hat{p}}$ and position $\hat{p}$ will be smooth, but the force estimate $\hat{W}^{\mathsf{B}}_{\mathsf{Pext}}$ will have a smaller bandwidth. Therefore the controller will react slower to the external force. If the observer gain is high, measurement noise and resolution steps from the measurements will show up in the observer velocity and position. The bandwidth of $\hat{W}^{\mathsf{B}}_{\mathsf{Pext}}$ will be bigger. The tuning of the observer gain can be done by state feedback tuning methods to obtain the right frequency and damping behavior.

Chapter 3

Test setup: Munin

The proposed model analysis and control method is applied to the parallel master device of a telemanipulation system, called "the Munin", at the Haptics lab of the Delft University of Technology (TU Delft).

The master device of the Munin is an overactuated (redundant) planar manipulator with three degrees of freedom: Translation in the x- and y-direction and rotation around the z-axis. The application of this setup is to operate a physical wrench to turn a bolt, which is an academic setup to test concepts. The manipulator has four legs, consisting out of three links, of which the third link is shared. This third link is the end effector, that will be moved by the operator. A picture of the Munin is shown, together with a schematic overview in figure 3-1. The slave device turning the bolt is not considered in this thesis, because desired dynamics are assumed to be known. A picture of the slave device is nonetheless shown in figure 3-2.

The Munin master device is actuated by four Maxon motors, connected to the four legs of the device by a 1:5.89 transmission consisting of disks, firmly connected by a cable that is wound around both disks. The inertia of the motor and the delivered torque for a certain current is obtained from the manufacturers data sheet. Because of the strong current sources that are used to control the motors, instead of voltage sources, the motor torque is assumed to be proportional to the control output. Optical encoders are mounted on top of the motors to measure the relative rotation with respect to the initialised position. The positions are initialised using switches at the outer positions of the first links.

The dimensions, masses, inertias and center of mass positions of all moving parts are obtained from the available computer model. Because of small differences between the 3d computer model and the real device some properties are measured. The lengths of all links and the masses and center of masses of the second links, the end effector and the second and third joints are measured.

All required data is shown in tabel 3-1.

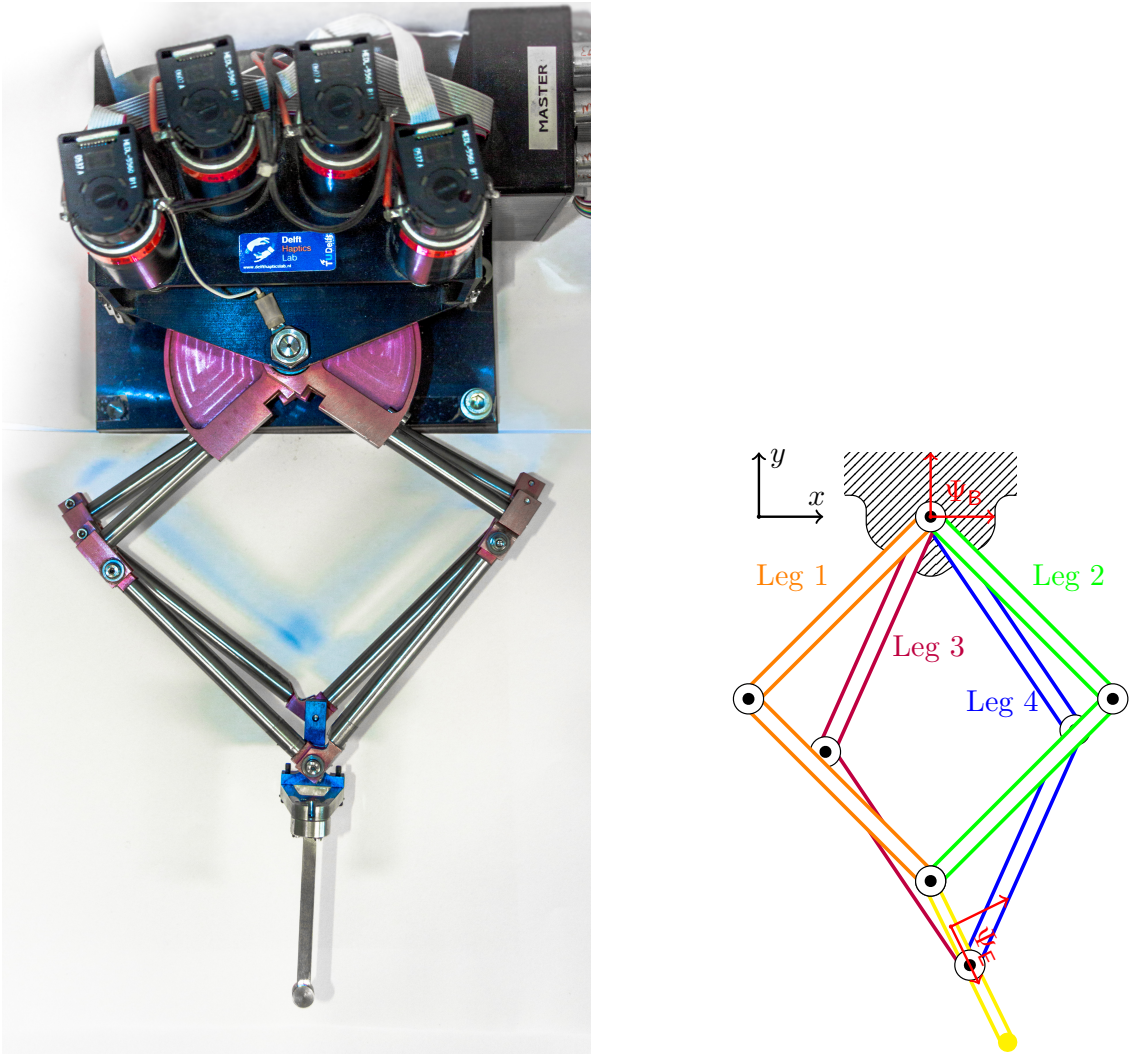

Figure 3-1: The Munin master device

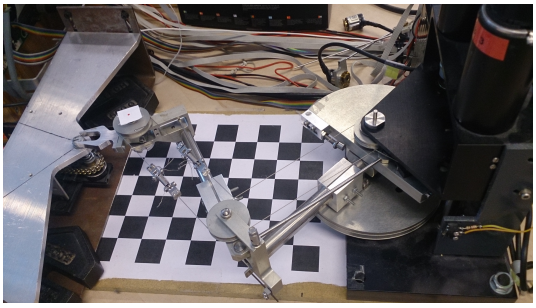

Figure 3-2: The munin slave device

Table 3-1: Relevant measures of the Munin

LINKS

link	**leg**	**distance between joints** [m]	**distance from first joint to center of mass** (joints on x axis) [m]	**mass** [g]	**inertia** (at the center of mass) 10^{-9} [kg·m^2]
1	1	0.1301	$x = 0.02785$ $y = -0.0156$	85.43	$\begin{bmatrix} 29931 & -14703 & -3599 \\ -14703 & 231810 & 184 \\ -3599 & 184 & 259523 \end{bmatrix}$
1	2	0.1301	$x = 0.02785$ $y = 0.0156$	85.43	$\begin{bmatrix} 29931 & 14703 & -3599 \\ 14703 & 231810 & -184 \\ -3599 & -184 & 259523 \end{bmatrix}$
1	3	0.1301	$x = 0.02785$ $y = -0.0156$	85.43	$\begin{bmatrix} 29931 & -14703 & -3599 \\ -14703 & 231810 & 184 \\ -3599 & 184 & 259523 \end{bmatrix}$
1	4	0.1301	$x = 0.02785$ $y = 0.0156$	85.43	$\begin{bmatrix} 29931 & 14703 & -3599 \\ 14703 & 231810 & -184 \\ -3599 & -184 & 259523 \end{bmatrix}$
2	1	0.1348	$x = 0.0736$ $y = 0$	22.6	$\begin{bmatrix} 378 & -16 & -14 \\ -16 & 31219 & -4 \\ -14 & -4 & 31218 \end{bmatrix}$
2	2	0.1291	$x = 0.0638$ $y = 0$	19.4	$\begin{bmatrix} 378 & 16 & -14 \\ 16 & 31219 & 4 \\ -14 & 4 & 31218 \end{bmatrix}$
2	3	0.1294	$x = 0.0638$ $y = 0$	19.4	$\begin{bmatrix} 378 & -16 & -14 \\ -16 & 31219 & -4 \\ -14 & -4 & 31218 \end{bmatrix}$
2	4	0.1341	$x = 0.0736$ $y = 0$	22.6	$\begin{bmatrix} 378 & 16 & -14 \\ 16 & 31219 & 4 \\ -14 & 4 & 31218 \end{bmatrix}$
3	all	0.0200	$x = 0.0380$ $y = 0$	40.2	$\begin{bmatrix} 9984 & 13 & 6872 \\ 13 & 26394 & 20 \\ 6872 & 20 & 18596 \end{bmatrix}$

JOINTS

All joints can only rotate around the z-axis. Therefore the unit twists of all joints are:

$$\hat{T}_{\mathsf{L}_{r,s}}^{\mathsf{J}_{r,s},\mathsf{J}_{r,s}} = \begin{bmatrix} 0 & 0 & 1 & 0 & 0 & 0 \end{bmatrix}^\top.$$

The masses of all second and third joints are 3.8 g and the inertias are assumed to be zero.

The mass of the first joints is set to zero (there will be no translational movement of this joint).

The inertia of the first joints is the gear ratio 5.89 times the sum of the inertia of the motor ($68.1 \cdot 10^{-7}$ kg·m^2) and the inertia of the total motor shaft ($4.2955 \cdot 10^{-5}$ kg·m^2):

$$I_{\mathsf{J}_{r,1},zz} = 5.89 \cdot \left(68.1 \cdot 10^{-7} + 4.2955 \cdot 10^{-5}\right)$$

Chapter 4

System model of the Munin

4-1 Kinematic relations

The model for the parallel haptic master device "the Munin" introduced in chapter 3 will be created using the methods introduced in chapter 2-1 in MATLAB®. The properties of the links and joints are shown in table 3-1. The configuration, the placement of all local coordinate systems, the definition of the joint angles, and the leg numbers are defined as presented in section 2-1-2 and are shown for the Munin in figure 4-1.

With this information the homogeneous matrices between all local coordinate systems can be created as a function of the angles $q_{r,t}$. An example for some of the homogeneous transformation matrices between the coordinate systems in leg 1 are:

$$H_{\mathsf{J}_{1,1}}^{\mathsf{L}_{1,1}} = \begin{bmatrix} \cos q_{1,1} & \sin q_{1,1} & 0 & 0 \\ -\sin q_{1,1} & \cos q_{1,1} & 0 & 0 \\ 0 & 0 & 1 & 0 \\ 0 & 0 & 0 & 1 \end{bmatrix}, \qquad H_{\mathsf{J}_{1,2}}^{\mathsf{L}_{1,2}} = \begin{bmatrix} \cos q_{1,2} & \sin q_{1,2} & 0 & 0 \\ -\sin q_{1,2} & \cos q_{1,2} & 0 & 0 \\ 0 & 0 & 1 & 0 \\ 0 & 0 & 0 & 1 \end{bmatrix}, \qquad H_{\mathsf{J}_{1,3}}^{\mathsf{L}_{1,3}} = \begin{bmatrix} \cos q_{1,3} & \sin q_{1,3} & 0 & 0 \\ -\sin q_{1,3} & \cos q_{1,3} & 0 & 0 \\ 0 & 0 & 1 & 0 \\ 0 & 0 & 0 & 1 \end{bmatrix},$$

$$H_{\mathsf{L}_{1,1}}^{\mathsf{J}_{1,2}} = \begin{bmatrix} 1 & 0 & 0 & -0.1301 \\ 0 & 1 & 0 & 0 \\ 0 & 0 & 1 & 0 \\ 0 & 0 & 0 & 1 \end{bmatrix}, \qquad H_{\mathsf{L}_{1,2}}^{\mathsf{J}_{1,3}} = \begin{bmatrix} 1 & 0 & 0 & -0.1348 \\ 0 & 1 & 0 & 0 \\ 0 & 0 & 1 & 0 \\ 0 & 0 & 0 & 1 \end{bmatrix}, \qquad H_{\mathsf{L}_{1,3}}^{\mathsf{L}_{3,3}} = \begin{bmatrix} 1 & 0 & 0 & -0.02 \\ 0 & 1 & 0 & 0 \\ 0 & 0 & 1 & 0 \\ 0 & 0 & 0 & 1 \end{bmatrix},$$

$$H_{\mathsf{B}}^{\mathsf{J}_{1,1}} = \begin{bmatrix} 1 & 0 & 0 & 0 \\ 0 & 1 & 0 & 0 \\ 0 & 0 & 1 & 0 \\ 0 & 0 & 0 & 1 \end{bmatrix}, \qquad H_{\mathsf{L}_{1,3}}^{\mathsf{P}} = \begin{bmatrix} \cos p_{\theta_z} & -\sin p_{\theta_z} & 0 & 0.01 \\ \sin p_{\theta_z} & \cos p_{\theta_z} & 0 & 0 \\ 0 & 0 & 1 & 0 \\ 0 & 0 & 0 & 1 \end{bmatrix} \qquad \text{for: } p_{\theta_z} = q_{1,1} + q_{1,2} + q_{1,3},$$

$$H_{\mathsf{B}}^{\mathsf{P}} = H_{\mathsf{L}_{1,3}}^{\mathsf{P}} H_{\mathsf{J}_{1,3}}^{\mathsf{L}_{1,3}} H_{\mathsf{L}_{1,2}}^{\mathsf{J}_{1,3}} H_{\mathsf{J}_{1,2}}^{\mathsf{L}_{1,2}} H_{\mathsf{L}_{1,1}}^{\mathsf{J}_{1,2}} H_{\mathsf{J}_{1,1}}^{\mathsf{L}_{1,1}} H_{\mathsf{B}}^{\mathsf{J}_{1,1}} = \begin{bmatrix} 1 & 0 & 0 & -p_x \\ 0 & 1 & 0 & -p_y \\ 0 & 0 & 1 & 0 \\ 0 & 0 & 0 & 1 \end{bmatrix}.$$

4-1-1 Inverse kinematics

The inverse kinematics for the Munin can be derived easily for this planar device. In general multiple solutions are possible, but in this case the configuration mode is known and so are

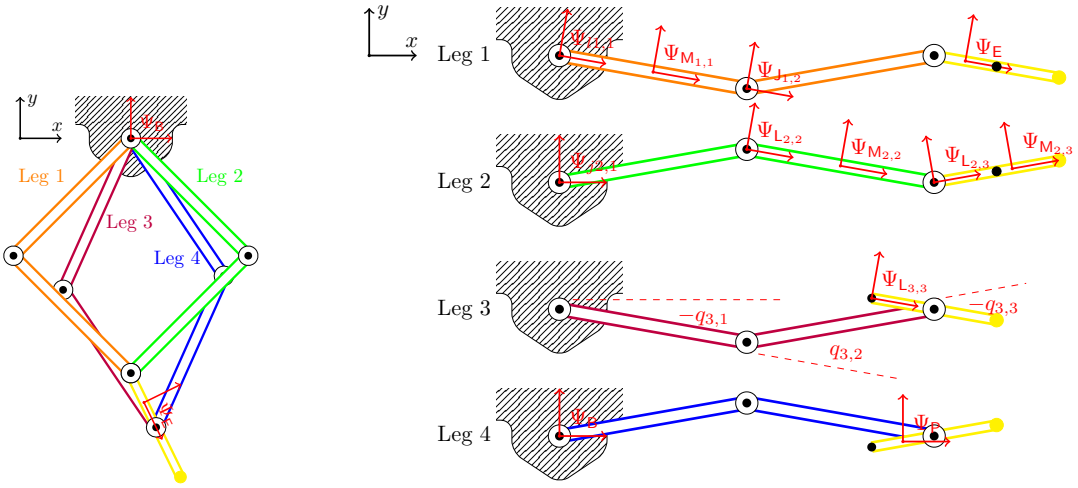

(a) Scheme of the Munin

(b) Seperate legs of the Munin

Figure 4-1: All local coordinate systems (Ψ) and angle names (q) for the Munin

the directions and ranges of all joints.

For a given end effector position (with the center of the end effector 1 cm from both joints),

$$p = \begin{bmatrix} 0 & 0 & p_{\theta_z} & p_x & p_y & 0 \end{bmatrix}, \tag{4-1}$$

the x and y positions of the origin $o^{\mathsf{B}}_{\mathsf{J}_{1,3}}$ of $\Psi_{\mathsf{J}_{1,3}}$ (expressed in Ψ_{B}) of leg 1 is found (equation 4-2):

$$\begin{aligned} o^{\mathsf{B}}_{\mathsf{J}_{1,3},x} &= p_x - 0.01 \cdot \sin p_{\theta_z}, \\ o^{\mathsf{B}}_{\mathsf{J}_{1,3},y} &= p_y - 0.01 \cdot \cos p_{\theta_z}. \end{aligned} \tag{4-2}$$

From these positions the angle $q_{1,2}$ is found using the cosine rule:

$$q_{1,2} = \frac{\cos^{-1}\left(0.1301^2 + 0.1348^2 - \left(\left(o^{\mathsf{B}}_{\mathsf{J}_{1,3},x}\right)^2 + \left(o^{\mathsf{B}}_{\mathsf{J}_{1,3},y}\right)^2\right)\right)}{2 \cdot 0.1301 \cdot 0.1348} - \pi. \tag{4-3}$$

The angle of the first joint $q_{1,1}$ is found using the cosine rule plus the angle from the Ψ_{B} to the position of $\Psi_{\mathsf{J}_{1,3}}$. The angle from the Ψ_{B} to the position of $\Psi_{\mathsf{J}_{1,3}}$ is computed using the inverse tangent (MATLAB function *atan2* to prevent division by zero):

$$q_{1,1} = \frac{\cos^{-1}\left(0.1301^2 - 0.1348^2 + \left(\left(o^{\mathsf{B}}_{\mathsf{J}_{1,3},x}\right)^2 + \left(o^{\mathsf{B}}_{\mathsf{J}_{1,3},y}\right)^2\right)\right)}{-2 \cdot \sqrt{\left(o^{\mathsf{B}}_{\mathsf{J}_{1,3},x}\right)^2 + \left(o^{\mathsf{B}}_{\mathsf{J}_{1,3},y}\right)^2} \cdot 0.1301} - \tan^{-1}\left(\frac{o^{\mathsf{B}}_{\mathsf{J}_{1,3},x}}{-o^{\mathsf{B}}_{\mathsf{J}_{1,3},y}}\right) + 2\pi. \tag{4-4}$$

The third angle $q_{1,3}$ as a function of p is now straightforwardly created, using the first two angles $q_{1,1}$ and $q_{1,2}$ and the end effector angle p_{θ_z}:

$$q_{1,3} = \frac{3}{2}\pi + p_{\theta_z} - (q_{1,1} + q_{1,2}). \tag{4-5}$$

Aside from some changes in the signs because of the configuration, the calculations for the other three legs is the same.

The homogeneous matrices, mass matrix and Jacobian matrices are constructed as functions of the joint angles q. The inverse kinematics will be used to make these functions dependent on the end effector position p, instead of on all angles q.

4-1-2 Forward kinematics

The forward kinematics of the Munin, describing the end effector position p as a function of the actuated joints $\begin{bmatrix} q_{1,1} & q_{2,1} & q_{3,1} & q_{4,1} \end{bmatrix}$, are found easily using goniometric methods, without the need for iteration methods, because the configuration is known and the system is planar.

Firstly, the positions of the second joints are found using the angle of the first joints and the length of the first links. For leg 1 this is:

$$o^{\mathsf{B}}_{\mathsf{J}_{1,2},x} = 0.1301 \cdot \cos q_{1,1}, \tag{4-6}$$
$$o^{\mathsf{B}}_{\mathsf{J}_{1,2},y} = 0.1301 \cdot \sin q_{1,1}. \tag{4-7}$$

After repeating this for all four legs, the positions of the third joint, which is shared for the first and the second leg, and for the third and the fourth leg, will be determined. The distance $d^{\mathsf{J}_{2,2}}_{\mathsf{J}_{1,2}}$ between the second joints of the first and second leg will be used, together with the known lengths of the second links, in the cosine rule to obtain the position of the third

joint:

$$d_{o^{\mathsf{B}}_{\mathsf{J}_{1,2}}}^{o^{\mathsf{B}}_{\mathsf{J}_{2,2}}} = \sqrt{\left(\left(o^{\mathsf{B}}_{\mathsf{J}_{2,2},x} - o^{\mathsf{B}}_{\mathsf{J}_{1,2},x}\right)^2 + \left(o^{\mathsf{B}}_{\mathsf{J}_{2,2},y} - o^{\mathsf{B}}_{\mathsf{J}_{1,2},y}\right)^2\right)}, \tag{4-8}$$

$$\beta = \cos^{-1}\left(\frac{0.1291^2 - 0.1348^2 - \left(d_{o^{\mathsf{B}}_{\mathsf{J}_{1,2}}}^{o^{\mathsf{B}}_{\mathsf{J}_{2,2}}}\right)^2}{-2 \cdot 0.1348 \cdot d_{o^{\mathsf{B}}_{\mathsf{J}_{1,2}}}^{o^{\mathsf{B}}_{\mathsf{J}_{2,2}}}}\right), \tag{4-9}$$

$$\gamma = \tan^{-1}\left(\frac{o^{\mathsf{B}}_{\mathsf{J}_{2,2},y} - o^{\mathsf{B}}_{\mathsf{J}_{1,2},y}}{o^{\mathsf{B}}_{\mathsf{J}_{2,2},x} - o^{\mathsf{B}}_{\mathsf{J}_{1,2},x}}\right), \tag{4-10}$$

$$o^{\mathsf{B}}_{\mathsf{J}_{1,3},x} = o^{\mathsf{B}}_{\mathsf{J}_{2,3},x} = o^{\mathsf{B}}_{\mathsf{J}_{1,2},x} + 0.1348 \cdot \cos(\beta - \gamma), \tag{4-11}$$

$$o^{\mathsf{B}}_{\mathsf{J}_{1,3},y} = o^{\mathsf{B}}_{\mathsf{J}_{2,3},y} = o^{\mathsf{B}}_{\mathsf{J}_{1,2},y} - 0.1348 \cdot \sin(\beta - \gamma). \tag{4-12}$$

These steps will be repeated for the third (shared) joint of the third and fourth leg. Finally, the end effector coordinates p_x, p_y and p_{θ_z} are determined:

$$p_{\theta_z} = \tan^{-1}\left(\frac{o^{\mathsf{B}}_{\mathsf{J}_{3,3},y} - o^{\mathsf{B}}_{\mathsf{J}_{1,3},y}}{o^{\mathsf{B}}_{\mathsf{J}_{3,3},x} - o^{\mathsf{B}}_{\mathsf{J}_{1,3},x}}\right), \tag{4-13}$$

$$p_x = o^{\mathsf{B}}_{\mathsf{J}_{3,3},x} + 0.01 \cdot \cos p_{\theta_z}, \tag{4-14}$$

$$p_y = o^{\mathsf{B}}_{\mathsf{J}_{3,3},y} + 0.01 \cdot \sin p_{\theta_z}. \tag{4-15}$$

These forward kinematics will be used to obtain the end effector position p from the measured (and actuated) joints.

4-1-3 Inverse Jacobian

The inverse Jacobian for the Munin, giving the rotational actuated joint velocities $\dot{q}$ as a function of the end effector twist $T_{\mathsf{P}}^{\mathsf{B},\mathsf{B}}$, is determined using equation 2-26. This Jacobian is a function of all joint coordinates and will be written as function of the end effector coordinates by replacing the joint coordinates by use of the inverse kinematics (equation 4-3, 4-4 and 4-5).

As an example the determination of the inverse Jacobian for leg 1 is shown here. The other legs will be analysed by the same method and the rows of the Jacobian matrix are chosen for its goal.

For all three joints ($t = \left\{ \begin{array}{ccc} 1, & 2, & 3 \end{array} \right\}$) in the leg, the unit twist is

$$\hat{T}_{\mathsf{L}_{1,t}}^{\mathsf{J}_{1,t},\mathsf{J}_{1,t}} = \begin{bmatrix} 0 & 0 & 1 & 0 & 0 & 0 \end{bmatrix}^\top, \tag{4-16}$$

(note: $\Psi_{\mathsf{J}_{1,1}}$ is Ψ_{B}), which will be written in base coordinates by the adjoint of the homogeneous matrix (equation 2-10):

$$\hat{T}^{\mathsf{B},\mathsf{J}_{1,1}}_{\mathsf{L}_{1,1}} = \begin{bmatrix}0 & 0 & 1 & 0 & 0 & 0\end{bmatrix}^\top, \tag{4-17}$$

$$\begin{aligned}\hat{T}^{\mathsf{B},\mathsf{J}_{1,2}}_{\mathsf{L}_{1,2}} &= Ad_{H^{\mathsf{B}}_{\mathsf{J}_{1,2}}} \cdot \begin{bmatrix}0 & 0 & 1 & 0 & 0 & 0\end{bmatrix}^\top \\ &= \begin{bmatrix}0 & 0 & 1 & 0.1301 \cdot \sin q_{1,1} & -0.1301 \cdot \cos q_{1,1} & 0\end{bmatrix}^\top,\end{aligned} \tag{4-18}$$

$$\hat{T}^{\mathsf{B},\mathsf{J}_{1,3}}_{\mathsf{L}_{1,3}} = Ad_{H^{\mathsf{B}}_{\mathsf{J}_{1,3}}} \cdot \begin{bmatrix}0\\0\\1\\0\\0\\0\end{bmatrix} = \begin{bmatrix}0\\0\\1\\0.13481 \cdot \sin\left(q_{1,1}+q_{1,2}\right) + 0.1301 \cdot \sin\left(q_{1,1}\right)\\-0.13481 \cdot \cos\left(q_{1,1}+q_{1,2}\right) - 0.1301 \cdot \cos\left(q_{1,1}\right)\\0\end{bmatrix}. \tag{4-19}$$

The wrench reciprocal to two of the three twists in the leg is chosen to be a linear force through the origin of the joints the wrench has to be reciprocal to. The moment around this line could be added, but will not for this device, because out-of-plane movements are constrained for the Munin. The wrench $W^{\mathsf{B}}_{1,1}$ to construct the Jacobian matrix line for the first joint of leg 1 will therefore be a linear force through the second and the third joint. A linear force through the origin in the x-direction can be written as a wrench: $\begin{bmatrix}0 & 0 & 0 & 1 & 0 & 0\end{bmatrix}$. (Without the out-of-plane constraints this wrench would be $\begin{bmatrix}1 & 1 & 0 & 1 & 0 & 0\end{bmatrix}$). Therefore, the linear force through the second and third joint of leg 1 will be written as:

$$\begin{aligned}\left(W^{\mathsf{B}}_{1,1}\right)^\top &= Ad^\top_{H^{\mathsf{L}_{1,2}}_{\mathsf{B}}} \cdot \left(W^{\mathsf{L}_{1,2}}_{1,1}\right)^\top \\ &= Ad^\top_{H^{\mathsf{L}_{1,2}}_{\mathsf{B}}} \cdot \begin{bmatrix}0 & 0 & 0 & 1 & 0 & 0\end{bmatrix}^\top \\ &= \begin{bmatrix}\cos\left(q_{1,1}+q_{1,2}\right) & \sin\left(q_{1,1}+q_{1,2}\right) & 0 & 0 & 0 & 0\\ -\sin\left(q_{1,1}+q_{1,2}\right) & \cos\left(q_{1,1}+q_{1,2}\right) & 0 & 0 & 0 & 0\\ 0 & 0 & 1 & 0 & 0 & 0\\ 0 & 0 & 0.1301\cdot\sin\left(q_{1,2}\right) & \cos\left(q_{1,1}+q_{1,2}\right) & \sin\left(q_{1,1}+q_{1,2}\right) & 0\\ 0 & 0 & 0.1301\cdot\cos\left(q_{1,2}\right) & -\sin\left(q_{1,1}+q_{1,2}\right) & \cos\left(q_{1,1}+q_{1,2}\right) & 0\\ 0.1301\cdot\sin\left(q_{1,1}\right) & -0.1301\cdot\cos\left(q_{1,1}\right) & 0 & 0 & 0 & 1\end{bmatrix}^\top \cdot \begin{bmatrix}0\\0\\0\\1\\0\\0\end{bmatrix},\end{aligned} \tag{4-20}$$

$$W^{\mathsf{B}}_{1,1} = \begin{bmatrix}0 & 0 & 0.1301 \cdot \sin\left(q_{1,2}\right) & \cos\left(q_{1,1}+q_{1,2}\right) & \sin\left(q_{1,1}+q_{1,2}\right) & 0\end{bmatrix}.$$

For the Jacobian matrix row for the second joint, a wrench representing the linear force through the first and third joint is required. Therefore, a homogeneous transformation matrix is constructed from the base coordinates Ψ_{B} to a new coordinate system $\Psi_{W^{\mathsf{B}}_{1,2}}$ located at the

base, rotated by φ such that the third joint is on the x axis of the coordinate system:

$$\varphi = \tan^{-1}\left(\frac{o^{\mathsf{B}}_{\mathsf{J}_{1,3},y}}{o^{\mathsf{B}}_{\mathsf{J}_{1,3},x}}\right), \tag{4-21}$$

$$H^{o^{\mathsf{B}}_{\mathsf{J}_{1,3}}}_{\mathsf{B}} = \left(e^{\begin{bmatrix}0 & 0 & 1 & 0 & 0 & 0\end{bmatrix}^{\top}\cdot\varphi} \cdot \begin{bmatrix}1 & 0 & 0 & 0\\ 0 & 1 & 0 & 0\\ 0 & 0 & 1 & 0\\ 0 & 0 & 0 & 1\end{bmatrix}\right)^{-1}, \tag{4-22}$$

$$\left(W^{\mathsf{B}}_{1,2}\right)^{\top} = Ad^{\top}_{\left(H^{o^{\mathsf{B}}_{\mathsf{J}_{1,3}}}_{\mathsf{B}}\right)} \cdot \left(W^{o^{\mathsf{B}}_{\mathsf{J}_{1,3}}}_{1,2}\right)^{\top}. \tag{4-23}$$

The wrench for the construction of the Jacobian of the third joint of the leg will be determined by the same method as was used for the first joint:

$$\left(W^{\mathsf{B}}_{1,3}\right)^{\top} = Ad^{\top}_{H^{\mathsf{L}_{1,1}}_{\mathsf{B}}} \cdot \left(W^{\mathsf{L}_{1,1}}_{1,3}\right)^{\top}. \tag{4-24}$$

The total inverse Jacobian matrix of the first leg J_1^{-1} is:

$$J_1^{-1} = \begin{bmatrix}\left(W^{\mathsf{B}}_{1,1}\cdot\hat{T}^{\mathsf{B},\mathsf{J}_{1,1}}_{\mathsf{L}_{1,1}}\right)^{-1}\cdot W^{\mathsf{B}}_{1,1}\\ \left(W^{\mathsf{B}}_{1,2}\cdot\hat{T}^{\mathsf{B},\mathsf{J}_{1,2}}_{\mathsf{L}_{1,2}}\right)^{-1}\cdot W^{\mathsf{B}}_{1,2}\\ \left(W^{\mathsf{B}}_{1,3}\cdot\hat{T}^{\mathsf{B},\mathsf{J}_{1,3}}_{\mathsf{L}_{1,3}}\right)^{-1}\cdot W^{\mathsf{B}}_{1,3}\end{bmatrix}, \tag{4-25}$$

$$\begin{bmatrix}\dot{q}_{1,1}\\ \dot{q}_{1,2}\\ \dot{q}_{1,3}\end{bmatrix} = J_1^{-1}\cdot T^{\mathsf{B},\mathsf{B}}_{\mathsf{P}}. \tag{4-26}$$

These steps will be repeated for all four legs of the Munin. Considering only the first terms of each Jacobian of each leg will result in the Jacobian for the actuated (first) joints:

$$J^{-1} = \begin{bmatrix}\left(W^{\mathsf{B}}_{1,1}\cdot\hat{T}^{\mathsf{B},\mathsf{J}_{1,1}}_{\mathsf{L}_{1,1}}\right)^{-1}\cdot W^{\mathsf{B}}_{1,1}\\ \left(W^{\mathsf{B}}_{2,1}\cdot\hat{T}^{\mathsf{B},\mathsf{J}_{2,1}}_{\mathsf{L}_{2,1}}\right)^{-1}\cdot W^{\mathsf{B}}_{2,1}\\ \left(W^{\mathsf{B}}_{3,1}\cdot\hat{T}^{\mathsf{B},\mathsf{J}_{3,1}}_{\mathsf{L}_{3,1}}\right)^{-1}\cdot W^{\mathsf{B}}_{3,1}\\ \left(W^{\mathsf{B}}_{4,1}\cdot\hat{T}^{\mathsf{B},\mathsf{J}_{4,1}}_{\mathsf{L}_{4,1}}\right)^{-1}\cdot W^{\mathsf{B}}_{4,1}\end{bmatrix}, \tag{4-27}$$

$$\begin{bmatrix}\dot{q}_{1,1}\\ \dot{q}_{2,1}\\ \dot{q}_{3,1}\\ \dot{q}_{4,1}\end{bmatrix} = J^{-1}\cdot T^{\mathsf{B},\mathsf{B}}_{\mathsf{P}}. \tag{4-28}$$

The constructed inverse Jacobian will be used to map torques at the joints to the end effector twist, and the end effector velocity to the joint velocities. Furthermore, the inverse Jacobian will be used in the projection of all inertias on a single inertia matrix at Ψ_{P}.

4-1-4 Forward Jacobian

The forward Jacobian matrix J which is the mapping between the actuated joint velocities and the end effector twist, is the pseudo inverse of the inverse Jacobian in equation 4-27. The forward Jacobian J_r that will map the joint velocities of a single leg r to the end effector twist can be found by the pseudo inverse of the inverse Jacobian in equation 4-25, but will be constructed analytically using the unit twists:

$$J_r = \begin{bmatrix} \hat{T}^{\mathsf{B},\mathsf{J}_{r,1}}_{\mathsf{L}_{r,1}} & \hat{T}^{\mathsf{B},\mathsf{J}_{r,2}}_{\mathsf{L}_{r,2}} & \hat{T}^{\mathsf{B},\mathsf{J}_{r,3}}_{\mathsf{L}_{r,3}} \end{bmatrix}. \tag{4-29}$$

4-2 Dynamics

A dynamic model of the Munin will be created using the masses (table 3-1) and the kinematic models derived in section 4-1. The standard form shown in equation 2-29 is altered to fit the Munin. $K(p)$ will be zero because there are no compliances in the relevant bandwidth of the system (all links and the transmission cables are assumed to be infinitely stiff) and there are no gravitational forces applying work to the system (all movements of the planar device are horizontal). Added to the equation are the friction forces in the first joints, because these forces are found to be significant in the response of the system.

4-2-1 Inertia matrix and the Coriolis wrench in workspace coordinates Ψ_{P}

All masses will be projected on the coordinate system Ψ_{P} which is parallel to Ψ_{B} and positioned at the end effector. This projection will be executed for all separate links and joints with their masses and inertias, which are shown in table 3-1, using equation 2-32. All the projected masses and inertias will be added, to create one position dependent 6×6 inertia matrix (equation 2-31).

To optimise the computational speed of the position-dependent inertia matrix the MATLAB® command *matlabFunction* is used. This function creates an optimised MATLAB® function with p as input (the joint coordinates q are replaced by workspace coordinates p by use of the inverse kinematics) and the inertia matrix at the present position as output, which will be used in the MATLAB® `Simulink`® model to control the Munin. A graphical interpretation of the inertia matrix at all positions is shown in appendix A.

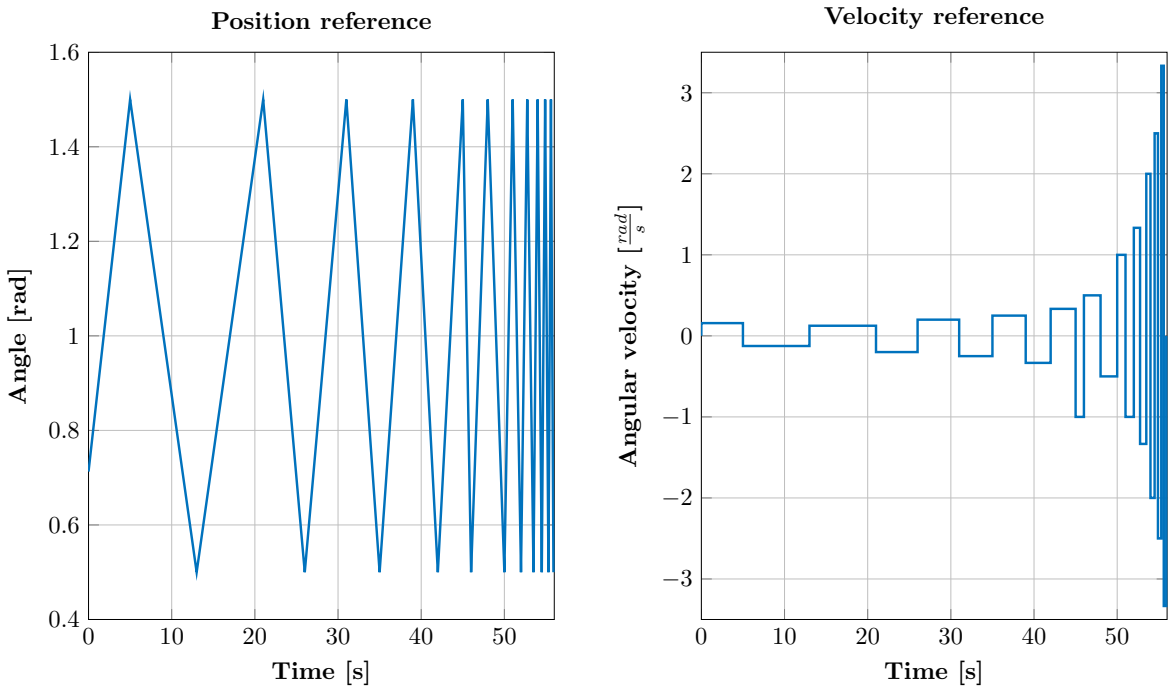

Figure 4-2: Friction data collection reference

The Coriolis wrench that would result from the Euler-Lagrange equation 2-39 could be computed analytically, but becomes too computationally complex to optimise with the MATLAB® function *matlabFunction*. Therefore the discrete derivative of the inertia matrix times the velocity of the end effector will be used to compute the Coriolis wrench.

4-2-2 Friction model

The Munin master system has significant friction in the first joints of each leg of the model, in which the friction of the motors and the transmission disks are included. The friction in the other joints of the system does not have significant influence on the dynamics of the system. Relevant data to model the friction is collected with the second links of each leg and the end-effector physically removed from the system.

The friction data collection consist of a PD controller controlling the first joints on several constant rotational velocities. The velocity and position references are shown in figure 4-2.

Taking the average of the control torque during the contant velocity interval (not including the first 0.2 seconds to discard the acceleration forces) yields a measure for the friction at that particular velocity. These friction forces are shown with the blue plus (+) signs in figure 4-3 for all tested velocities, for all motors. The red line shows the interpolated friction data used in the system model. This uses the average of several runs, discarding the points that are to close to zero velocity, to be used in a discrete simulation with a sample time $Ts = 0.001$

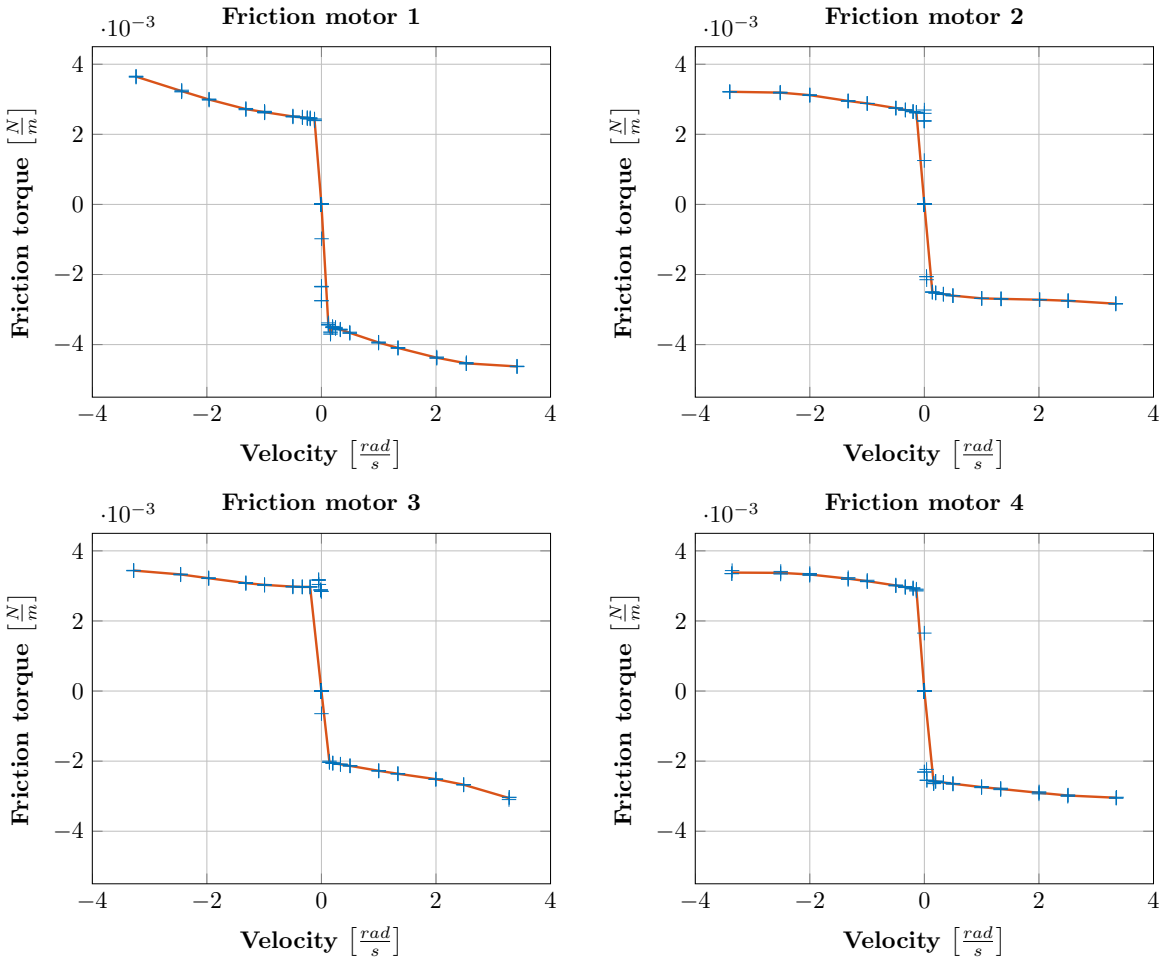

Figure 4-3: Friction

second. (The points too close to zero velocity cause oscillations because the friction torque will cause the system to change the velocity direction within one sample time). The red line represents the look-up table that will be used in the model of the system to obtain the friction torques.

Repeating the data collection to obtain the friction data does not lead to significant changes, which suggests the friction data is reliable. Replacing the cables connecting the disks between the motor and the first joint does change the friction model significantly. Therefore the friction data has to be updated if one of the cables is replaced.

Chapter 5

Controller

5-1 Observer

An observer is used to obtain the twist of the end effector with respect to the base and the external wrench applied to the end effector by the human operator.

The structure of the observer is built up in MATLAB® `Simulink`® as suggested in chapter 2-2. Because there are no stiffness forces acting on the Munin, $\tilde{K}(p)$ is left out of the observer (there are no gravitational or stiffness forces working on the system). The continuous time integration in equation 2-51 and 2-52 are implemented using discrete integrators: $\frac{Ts}{z-1}$.

The friction forces will change a lot for small velocities of the first joints (figure 4-3). To prevent undesired behavior that can result from these quick changes in combination with discrete integration, the friction effects will be removed from the observer and from the control torque entering the observer. The friction compensation will remain in the control torque applied to the real system.

The observer gains are static and are computed using the pole placement *place($A^\top$,$C^\top$,desired poles)* command in MATLAB®. The state space system used for the pole placement is a pure integrator, with only the position as output. This is represented in a state space representation to be used in the pole placement command. $A = \left[\begin{smallmatrix} 0 & 1 \\ 0 & 0 \end{smallmatrix}\right]$ and $C = [\,1\ 0\,]$ for the state $x = \left[\begin{smallmatrix} p \\ \dot{p} \end{smallmatrix}\right]$. $B = \left[\begin{smallmatrix} 0 \\ M^{-1}(p) \end{smallmatrix}\right]$ and $D = [0]$ are not relevant for the pole placement of the observer gain, because the observer gain adds input and obtains output directly from the states.

The poles that are chosen define how quickly the observer corrects for errors between the real system end effector position, and the position of the end effector of the observer. Making this correction slow will result in a smoother velocity and force estimate, but creates more (phase) lag between the real and estimated values and therefore in the controller reaction to

external forces. Making the correcting faster results in less delay, but also in more influence of the steps caused by the sensor resolution. Those steps are especially large for the angle of the end effector p_{θ_z}, because of the mechanical structure of the Munin. The optimal poles are found by a manual iterative process.

To determine the observer gains using MATLAB®'s *place*, desired poles are created by a desired system frequency ω and damping ratio ζ. The values for ω and ζ are taken as high as possible, while making sure the steps caused by the resolution of the encoders does not show up in the response of the observer. For p_{θ_z} the values are $\omega = 10\text{Hz} = 20\pi\frac{\text{rad}}{\text{s}}$ and $\zeta = 0.5$, and for p_x and p_y the frequency and damping ratio are $\omega = 20\text{Hz} = 40\pi\frac{\text{rad}}{\text{s}}$ and $\zeta = 0.5$. Therefore, the observer gain L is:

$$L = \begin{bmatrix} L_{\dot{p}} \\ L_{\ddot{p}} \end{bmatrix} = \begin{bmatrix} 3947.4 & 0 & 0 \\ 0 & 15796 & 0 \\ 0 & 0 & 15796 \\ 62.8165 & 0 & 0 \\ 0 & 125.7119 & 0 \\ 0 & 0 & 125.7119 \end{bmatrix}. \tag{5-1}$$

For the observer error $e_{\hat{p}} = p - \hat{p}$. (Note: for the convenience of the notation in equation 5-1, p and $\hat{p}$ are reduced to a 3×1 vector by removing the zeros from the actual 6×1 vector for the constrained directions p_{θ_x}, p_{θ_y} and $p_z \Rightarrow p = \begin{bmatrix} p_{\theta_z} & p_x & p_y \end{bmatrix}^\top$.)

To estimate the external wrench applied to the end effector by the human operator, the outcome of the observer gains times the observer error will be used:

$$\hat{W}^{\mathsf{B}}_{\mathsf{Pext}}(e_{\hat{p}}) = \tilde{M}(p) \cdot \left(L_{\ddot{p}} \cdot e_{\hat{p}} + L_{\dot{p}} \cdot \dot{e}_{\hat{p}} \right). \tag{5-2}$$

Because the derivative on the outcome of the observer gain will still contain the sensor resolution steps (and will be performed in discrete time: $\frac{z-1}{Ts}$), this value will be filtered by a second order filter B. This filter is a second order system with an eigenfrequency of 10Hz and a damping ratio of 0.8:

$$B = \frac{0.001909z + 0.001847}{z^2 - 1.901z + 0.9048}. \tag{5-3}$$

A scheme for the observer including the external wrench estimation is shown, together with the controller, as a block diagram in figure 5-1. The bottom part of this diagram is the observer and the force estimator, with the measured end effector position p and the end effector control wrench $W^{\mathsf{B}}_{\mathsf{P\,c}}$ as input and the velocity $\hat{\dot{p}}$ and external wrench $\hat{W}^{\mathsf{B}}_{\mathsf{Pext}}$ as outputs.

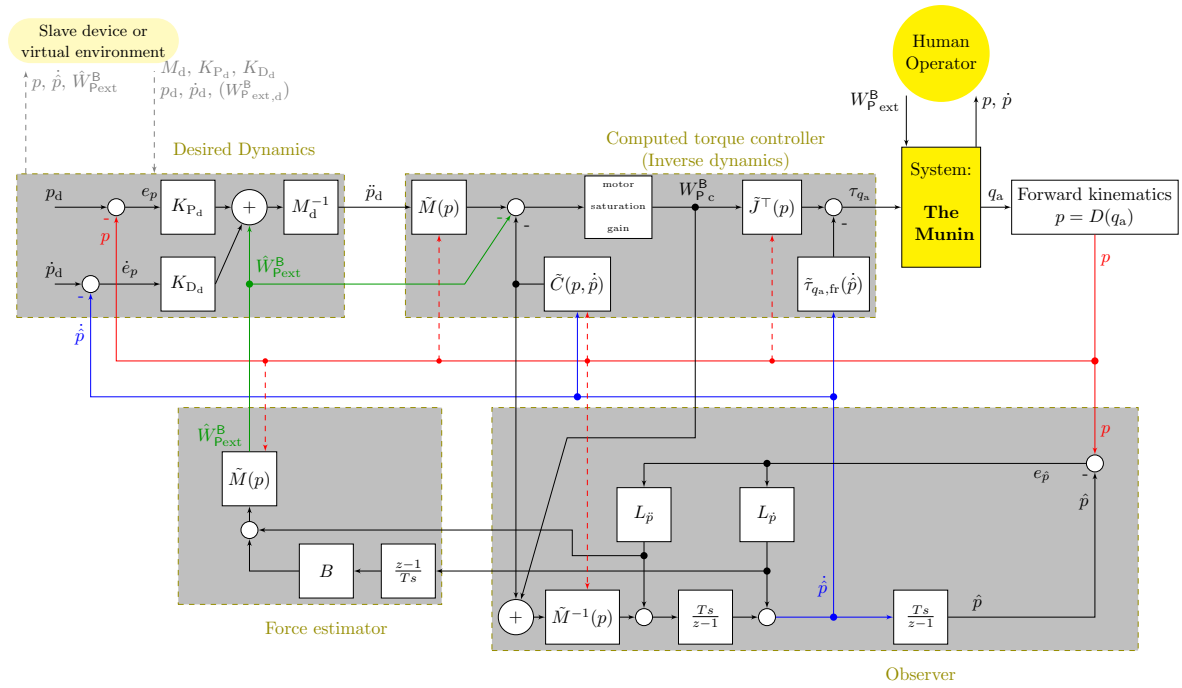

Figure 5-1: The Controller block diagram as implemented on the Munin

5-2 Controller

The control algorithm introduced in section 2-2 in equation 2-40 together with equation 2-42 is implemented on the system by use of MATLAB® `Simulink`®.

The control algorithm in equation 2-40 is altered to fit the Munin by removing the non-present $\tilde{K}(p)$ and adding compensation $\tilde{\tau}_{q_{\mathrm{a}},\mathrm{fr}}(\dot{\hat{p}})$ for the friction in the first joints $\tau_{q_{\mathrm{a}},\mathrm{fr}}(\dot{p})$:

$$\tau_{q_{\mathrm{a}}} = \tilde{J}^{\top}(p)\left(\tilde{M}(p)\cdot\underbrace{\left(M_{\mathrm{d}}^{-1}\cdot\left(\hat{W}^{\mathsf{B}}_{\mathsf{Pext}} + K_{\mathrm{P_d}}\cdot e_p + K_{\mathrm{D_d}}\cdot\dot{e}_p\right)\right)}_{\ddot{p}_{\mathrm{d}}} + \tilde{C}(p,\dot{\hat{p}}) - \hat{W}^{\mathsf{B}}_{\mathsf{Pext}}\right) - \tilde{\tau}_{q_{\mathrm{a}},\mathrm{fr}}(\dot{\hat{p}}). \tag{5-4}$$

A motor control saturation of 2.5 A $\Rightarrow \tau_{q_{\mathrm{a}}\max} = 2.5 \cdot 0.0389 = 0.09725$ Nm for each motor is taken into account. With the transmission between the motor and the first joint this is a maximum of $0.09725 \cdot 5.89 = 0.5728$ Nm at the first/actuated joints. To preserve the direction of the end effector control wrench $W^{\mathsf{B}}_{\mathsf{P}\,c}$ all motor torques are reduced by the same gain needed to saturate the value of the motor with the highest control torque. This gain is shown in figure 5-1: the *motor saturation gain* block.

The total control algorithm used to control the Munin, including the observer to estimate the velocity and the external force, is shown in the block diagram in figure 5-1.

Chapter 6

Validation Results

The control algorithm, as described in the previous sections, is applied to the Munin and the generated data is collected in order to validate whether the controller works as expected and to obtain the boundaries of the possible desired dynamics quantities M_d, $K_{\mathrm{P_d}}$ and $K_{\mathrm{D_d}}$. The collected data will be shown in this chapter. The response data will be presented in two types of plots. The first plot will show the position (y-axis) of the end effector over time (x-axis). The second plot is a phase plot of the same response data. This plot will show the position (x-axis) versus the velocity (y-axis). The expected movement through this phase plot for every initial position and velocity is shown with a vector field, representing the desired dynamics (M_d, $K_{\mathrm{P_d}}$and $K_{\mathrm{D_d}}$) used in the controller.

6-1 Test: The Computed Torque Controller

At first, the force estimation is manually set to zero and no external forces will act on the system, to test the computed torque control part as position controller. Step responses in all three workspace coordinates p_{θ_z}, p_x and p_y are performed individually. This results in knowledge of the possible range of the $K_{\mathrm{P_d}}$ and $K_{\mathrm{D_d}}$ values. The lower boundaries are a result of the non-perfect friction compensation. The maximum values are bounded by the demand of stable behavior and therefore by the sensor resolution, sample time, observer gain and differences between the model and the real system.

The maximum damping mass ratio $M_\mathrm{d}^{-1}K_{\mathrm{D_d}}$, which appears to be the main limitation of the controller, was found to be

$$\max\left(M_\mathrm{d}^{-1}K_{\mathrm{D_d}}\right) = \frac{50\frac{\mathrm{N\cdot s}}{\mathrm{m}}}{0.2\mathrm{kg}} = 250\frac{1}{\mathrm{s}}, \tag{6-1}$$

in the p_x and p_y direction, and

$$\max\left(M_\mathrm{d}^{-1}K_{\mathrm{D_d}}\right) = \frac{0.01\frac{\mathrm{N\cdot m\cdot s}}{\mathrm{rad}}}{6.389\cdot 10^{-5}\mathrm{kg}\cdot\mathrm{m}^2} = 156.5\frac{1}{\mathrm{rad}\cdot\mathrm{s}} \tag{6-2}$$

in the p_{θ_z}direction. These values are found by a manual iterative process, keeping the system stable and not oscillating.

The maximal stiffness mass ratio $M_{\mathrm{d}}^{-1}K_{\mathrm{P_d}}$ is chosen to let the maximal damping be the critical damping ($\zeta = 1$):

$$\max\left(M_{\mathrm{d}}^{-1}K_{\mathrm{P_d}}\right) = \frac{3158\frac{\mathrm{N}}{\mathrm{m}}}{0.2\mathrm{kg}} = 15790\frac{1}{\mathrm{s}^2} \tag{6-3}$$

for p_x and p_y and

$$\max\left(M_{\mathrm{d}}^{-1}K_{\mathrm{P_d}}\right) = \frac{4.26\cdot 10^{-4}\frac{\mathrm{N\cdot m}}{\mathrm{rad}}}{6.389\cdot 10^{-5}\mathrm{kg}\cdot\mathrm{m}^2} = 6667.725\frac{1}{\mathrm{rad}\cdot\mathrm{s}^2}, \tag{6-4}$$

in the p_{θ_z} direction.

Step responses are tested on the system in p_x, p_y and p_{θ_z}, for the maximal stiffness of $3158\frac{\mathrm{N}}{\mathrm{m}}$ and $4.26\cdot 10^{-4}\frac{\mathrm{N\cdot m}}{\mathrm{rad}}$, 0.2 times the maximal stiffness and 0.01 times the maximal stiffness respectively. All three stiffness matrices $K_{\mathrm{P_d}}$ are tested with three damping values, such that the damping ratio ζ is 1, 0.5 and 0.2. All plots of these nine tests can be found in appendix B. With the high stiffness values the controller fails to fulfill the desired dynamics because of motor saturation (plot lines will be shown in red while the motors saturate), for the step responses of 5cm and 0.5rad. Closer to the reference position 0 the system will follow the desired dynamics. For the low controller stiffness an error remains because of the friction.

To show the influence of taking the friction and the non-linear mass into account in the controller, step responses with and without friction compensation and mass linearisation are performed on the system with

$$K_{\mathrm{P_d}} = \begin{bmatrix} 0.085 & 0 & 0 \\ 0 & 640 & 0 \\ 0 & 0 & 640 \end{bmatrix}, \tag{6-5}$$

$$K_{\mathrm{D_d}} = \begin{bmatrix} 0.0023 & 0 & 0 \\ 0 & 11.3 & 0 \\ 0 & 0 & 11.3 \end{bmatrix}, \tag{6-6}$$

$$M_{\mathrm{d}} = \begin{bmatrix} 0.0000639 & 0 & 0 \\ 0 & 0.2 & 0 \\ 0 & 0 & 0.2 \end{bmatrix}, \tag{6-7}$$

and are shown in figure 6-1 (0.2 times the maximal stiffness and a damping ratio $\zeta = 0.5$). For each step response four plots are shown: The response in the direction of the step over time, the phase plot of this same response and the response in the other two directions of p_x, p_y and p_{θ_z} to show the cross correlation in the response and the limitation of this effect while taking the non linear mass matrix into account in the control algorithm. In the ideal case a step in a certain direction would follow the chosen desired dynamics and no response on this step wil show up in the other directions. From the plots it can be seen that the implementation of the friction compensation and mass linearisation by the controller have a positive effect towards this goal.

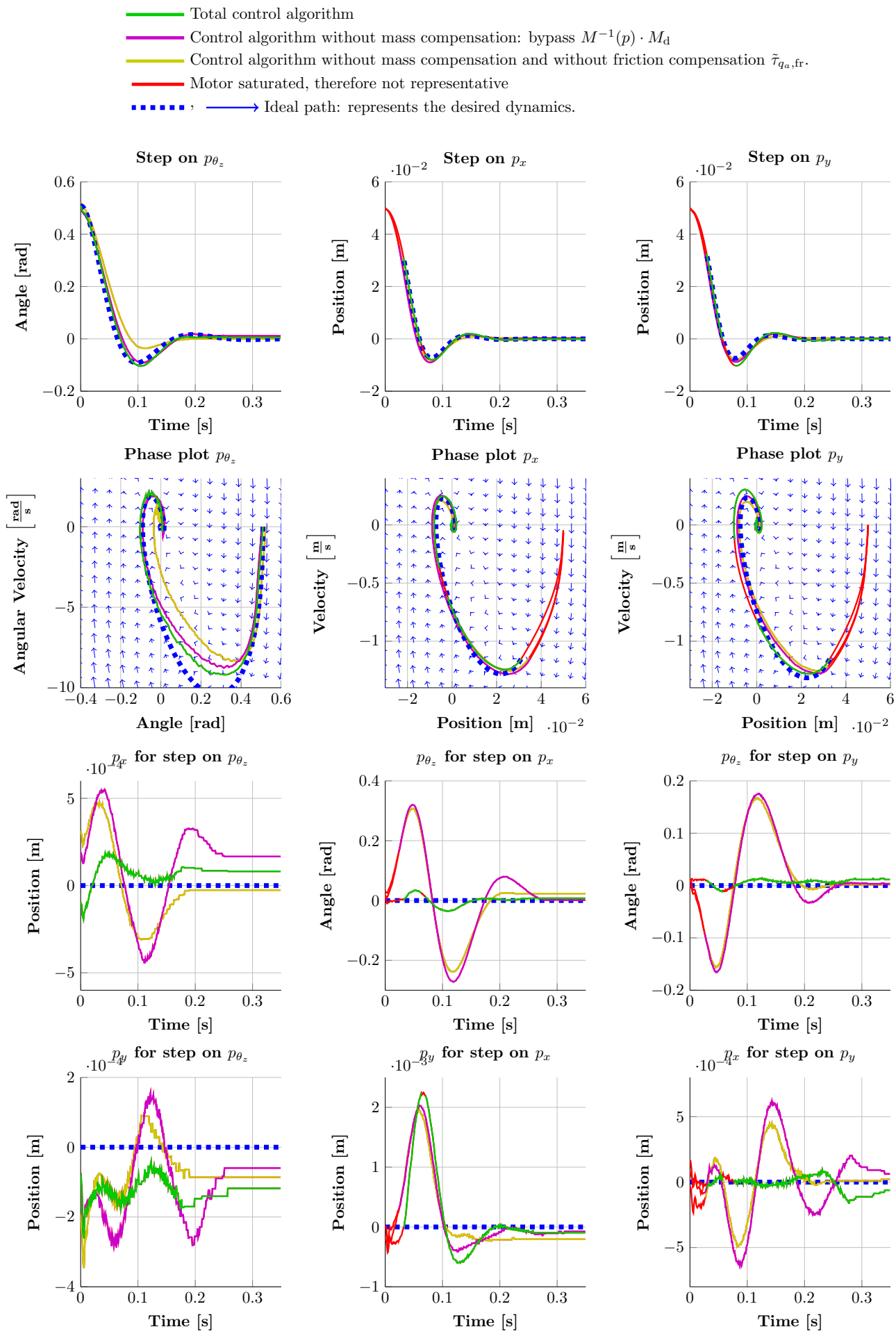

Figure 6-1: Response of a reference step of 0.5 rad on p_{θ_z} (left), 5cm on p_x (middle) and 5cm on p_y (right). The top two graphs shows the response of the direction of the step. The lower two graphs shows the response in the other directions (cross coupling). Responses are shown for the total controller, the controller without mass compensation, the controller without mass and friction compensation, and the ideal (simulated) response for the desired dynamics.

6-2 Test: Static estimation of the external wrench

The next validation stage will validate the estimation $\hat{W}^{\mathsf{B}}_{\mathsf{P}_{\text{ext}}}$ of a static (0 Hz) external wrench $W^{\mathsf{B}}_{\mathsf{P}\,\text{ext}}$. Therefore, a known static external force is applied to the end effector that will be compared to the force estimate of the observer. The external force is created by a spring (figure 6-2), with a known spring constant k_{ext} and known positions of the attachment point (static with respect to Ψ_{B}).

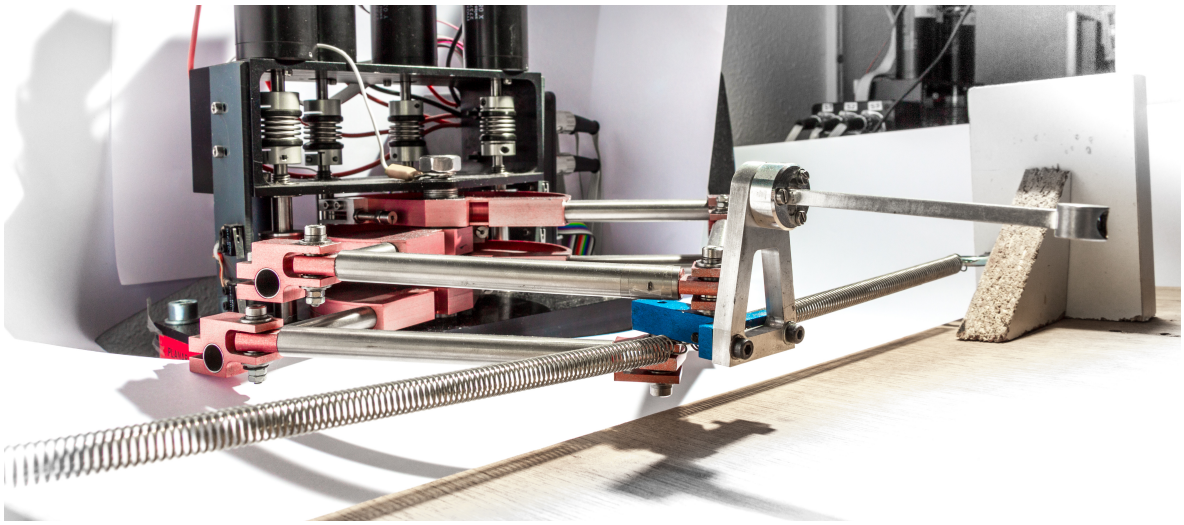

Figure 6-2: External springs are attached to the end effector in the p_x direction

The estimation of the external forces is tested in the directions of p_x and p_y. The end point of the attached external spring is moved in steps of three centimeter, while the controller keeps the end effector in place. Therefore the external force difference is known and can be compared to the difference in the force estimation. In table 6-1 the measurements are shown together with the estimated forces and the errors in those estimations. The errors are expected to be caused by the static friction that is not compensated at very low velocities. The factor two difference between the p_x and the p_y directions is a result of the two springs used in the p_x direction and one spring in the p_y direction. The spring constant for one spring is $59\frac{\text{N}}{\text{m}}$ (The spring constant is obtained by measuring the time for hundred oscillations with a load of 0.5 kg).

6-3 Test: Change the virtual desired end effector mass M_{d}

The last validation stage is to test the ability of the controller to change the virtual desired mass M_{d}. The $K_{\text{P}_{\text{d}}}$ and $K_{\text{D}_{\text{d}}}$ will be set to zero and desired masses will be chosen to investigate the range of possible desired masses (only diagonal M_{d} matrices will be considered). External springs (with known spring constants k_{ext}) are attached to the end effector (figure 6-2). From a initial position, different from the equilibrium position of the external springs, the end effector will oscillate around the equilibrium position of the external springs. The oscillation

Table 6-1: Static force estimations

Direction	Real force [N]	Force estimate [N]	Force estimation error [N]	Force estimation error precentage [%]
p_x	3.0070	2.8888	-0.1182	-3.9
p_x	3.1101	2.3301	-0.7800	-25.1
p_x	3.1256	2.2461	-0.8795	-28.1
p_x	3.0155	2.8428	-0.1727	-5.7
p_y	1.6401	1.4084	-0.2316	-14.1
p_y	1.6235	1.5880	-0.0355	-2.2
p_y	1.6063	1.7740	0.1677	10.4
p_y	1.6244	1.5780	-0.0465	-2.9
p_y	1.6552	1.2448	-0.4104	-24.8
p_y	1.6112	1.7216	0.1104	6.9
p_y	1.6270	1.5504	-0.0766	-4.7
p_y	1.6374	1.4368	0.2006	12.3

frequency will be compared to the expected frequency for the desired mass and the known external spring constant,

$$\omega = \sqrt{\frac{k_{\mathrm{ext}}}{M_{\mathrm{d}}}}. \tag{6-8}$$

This will be tested for the p_x and p_y directions separately.

Changing the desired mass of the end effector in the controller will let the the Munin respond differently to external forces. Without a controller stiffness and damping ($K_{\mathrm{P_d}} = 0$ and $K_{\mathrm{D_d}} = 0$), three different desired masses M_{d} shown in table 6-2, are tested in x and y direction. In figure 6-3 the responses are shown. From this responses it can be seen that for a higher desired mass, unexpected damping is added to the system, although this damping is small: The system will keep oscillating for at least half a minute. With a fast Fourier transform (FFT) on the measured position data, the frequency data is obtained and also shown in figure 6-3 and table 6-2. From the plot, in which the expected frequencies are shown by the vertical lines, and in the table, it can be seen that the response frequencies are slightly smaller, but close to the expected frequencies.

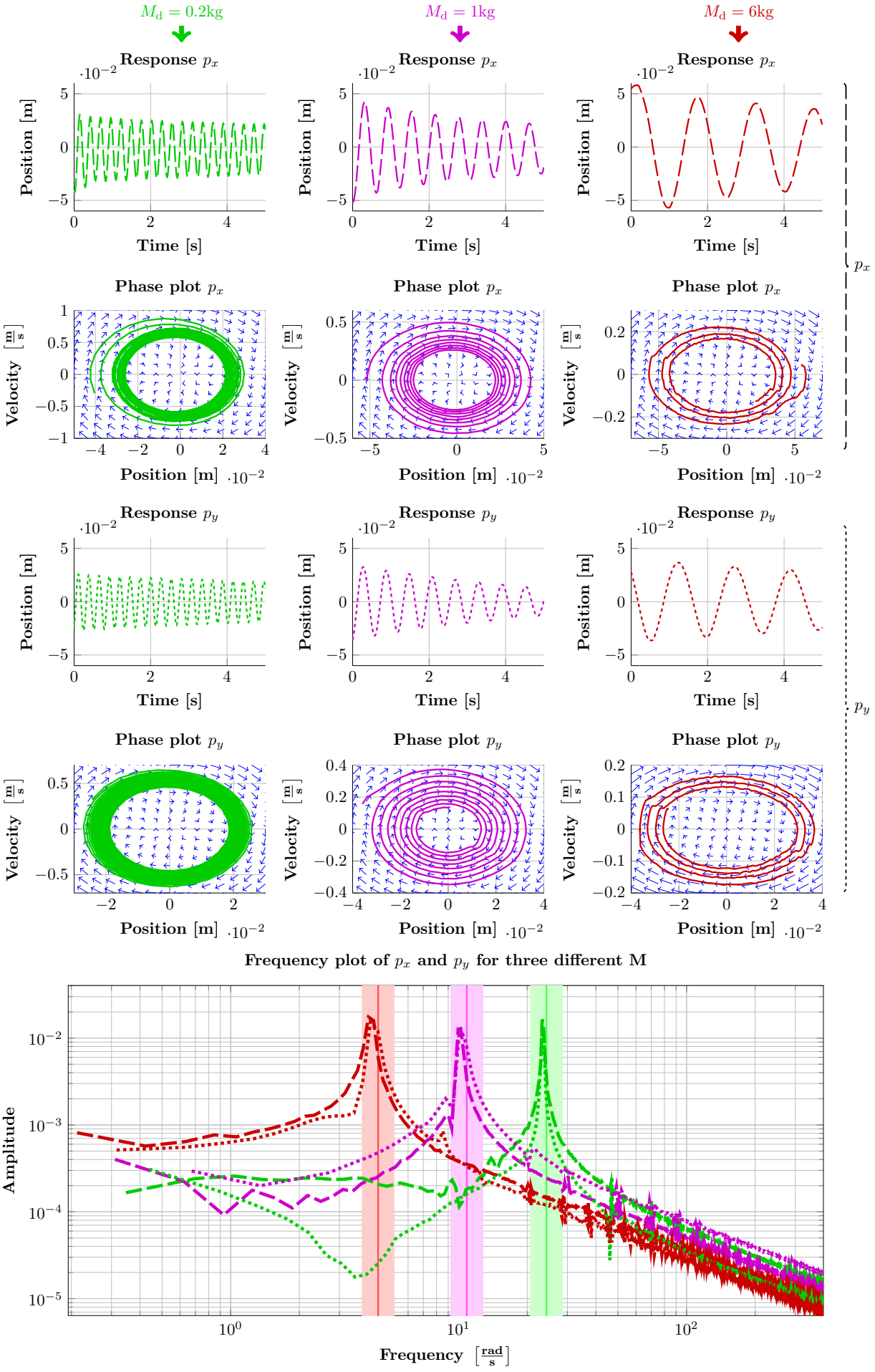

Figure 6-3: Response for a controlled desired mass at the end effector of 0.2kg (green), 1kg (purple), and 6kg (red) oscillating between two external springs. Response tested for p_x (top two graphs and dashed) and p_y (middle graphs and dotted). In the lower graph the frequency content (FFT) is shown for all cases. The vertical lines will show the expected frequency.

Table 6-2: Desired masses, the expected response frequencies and the most dominant frequency in the FFT of the measurements

$M_\mathbf{d}$ [kg]	**Expected frequency with a external spring constant of 118 $\frac{\mathbf{N}}{\mathbf{m}}$** $\left[\frac{\text{rad}}{\text{s}}\right]$	**Dominant frequency in the p_x direction** $\left[\frac{\text{rad}}{\text{s}}\right]$	**Frequency p_x error percentage** [%]	**Dominant frequency in the p_y direction** $\left[\frac{\text{rad}}{\text{s}}\right]$	**Frequency p_y error percentage** [%]
0.2	$\sqrt{\frac{118}{0.2}} = 24.29$	23.26	4.25	23.27	4.20
1	$\sqrt{\frac{118}{1}} = 10.86$	9.95	8.40	10.11	6.89
6	$\sqrt{\frac{118}{6}} = 4.43$	4.02	9.15	3.79	14.48

Chapter 7

Discussion

7-1 Controller performance

The goal was to implement an admittance controller to parallel haptic master systems without a force sensor. The proposed structure was implemented and tested on the Munin, a 3-degrees-of-freedom planar parallel haptic master device. The controller performs properly and as expected. The limits of the range of possible desired dynamic quantities that can be projected on the end effector is explored by trail and error. This range is found to be large enough to project a reasonable range of desired dynamics.

Force estimation compared to a force sensor, has the disadvantage that high frequency force differences will not be detected. The advantage, besides the significant reduction of costs, is that the force sensing does not include the low frequency disadvantages of force sensors, for example drift and hysteresis. Furthermore, it is an advantage that the external force can be applied anywhere on the device, contrary to a force sensor, which only measures the force in one point. Future research could result in better knowledge about the quality of the force estimate, by adding a force sensor to the end effector to measure the external force and compare this measurement to the estimated force for different external force frequencies. This measurement data would provide knowledge about the bandwidth of the force estimation. It has to be noted that a good force estimate requires a back-drivable system and an accurate system model.

The model used in the controller structure can still be improved in the computation of the Coriolis forces, the friction compensation and the external force estimation. The used Coriolis tensor is not complete, because only the discrete time derivative of the mass matrix times the velocity is taken into account, neglecting the term $\frac{1}{2}\dot{p}^\top \frac{\partial M(p)}{\partial p}\dot{p}$. This will have a small influence on the system when moved by the human operator, because this movement will only contain relatively small velocities. However, in the high velocities during the position control tests, it can be seen in figure 6-1 that the system does still have a relatively large

response in the p_y direction while a step on the reference of p_x is performed. The friction compensation and the force estimation are performed using a relative simple method. These are both extensive research areas and therefore are expected to be open to improvement in the used control algorithm.

A range of desired dynamics can be projected on the system. The desired damping gain $K_{\mathrm{D_d}}$ and therefore also the desired stiffness gain $K_{\mathrm{P_d}}$ is limited because of the response speed of the observer to an observer error. This speed is determined by the observer gains, which are limited by the quality (resolution) of the sensors with their mapping (determined by the kinematics) to the end effector coordinates. Therefore the range of the possible desired dynamics to be projected on the end effector, can be improved by improvements of the kinematic design and the sensors.

Other future work to improve the control algorithm, applied to implement an admittance controller without force sensor to the parallel haptic master device, can include extensive deterministic stability research. This will lead to a description that can be used in optimization algorithms on the observer gains, with performance criteria chosen to enable a larger range of possible projected desired dynamics.

7-2 Application of the control algorithm

The implemented control algorithm will act as a local (on the master device) admittance controller. In general an admittance controller receives a force as input and has a velocity (and therefore position) as output, contrary to an impedance controller, which receives a velocity (and position) as input and creates a reaction force. Although, because of measuring the positions and generating a control wrench to the end effector, it can be interpreted as impedance controller, in this thesis the estimated force is assumed as input to generate an end effector velocity and position as output, to admit to the applied force. Therefore, this controller for a parallel haptic master device is an admittance controller.

This thesis has focused on the control of a haptic master device, which would in a telemanipulation system be integrated with a bilateral controller, which connects the master and slave device. The observer makes both velocity and interaction force available to the bilateral controller (which controls the coupling of the master and slave devices). Therefore, the developed admittance controller allows many variations of bilateral control. While taking the whole telemanipulation system into account, the bilateral controller can be chosen to act as impedance, admittance, or four channel controller, depending on the choice of information exchange to and from the slave device and/or the virtual environment. The admittance controller enables the freedom to shape the desired dynamics (which have to be stable and in a within certain limits), to be experienced by the operator. This can be used to project, for instance, an estimation of the dynamics at the environment of a position-controlled slave device, on the end effector of the master. This would create an impedance controller, considering the whole telemanipulation device, because the position is sent to the slave device and

a force (described by the desired dynamics) is sent back to the master device.

Physical interaction with an object is typically expressed using a mass-spring-damper system. Because the desired dynamics are defined in the commonly used SI units, they are intuitive to interpretation. This will be convenient in shaping haptic shared control [33] or model-mediated control [34], that will guide or repel the operator to or from certain paths and points, possibly based on model knowledge of the slave's environment. The admittance controller not only allows the stiffness and damping, but also the mass to be shaped for haptic shared control guidance strategies.

Because the force estimation has the advantage that it estimates the interaction of the complete master device with the environment, and not just at a specific point, which is the case when a force sensor is used, the device can react on collisions of one of the links or joints into, for example, a human. Therefore, it enables safer operation in collaboration with a human, without the need of an artificial skin to measure the force everywhere on the device. This will also be true for other kinds of collaborative robotics outside the scope of teleoperational applications, when using force estimation instead of force measurement. Although, it has to be noted that, contrary to an artificial skin, all forces applied somewhere on the device will be recognized by the force estimator as a force at the end effector.

Chapter 8

Conclusion

The goal of the research presented in this thesis is to design and test an admittance controller for a parallel haptic master device, without the use of a force sensor. For this goal a controller structure has been presented and tested.

The proposed control algorithm extends the traditional computed torque controller, which compensates for the non-linear dynamics of the parallel mechanism. Firstly, the computed torque controller is combined with desired dynamics, to shape the desired acceleration. Secondly, an observer to obtain velocity and external force information is added. The complete algorithm is successfully implemented on the test setup; the Munin (a 3-degrees-of-freedom planar parallel haptic master device). From the measurements, the algorithm shows to be able to project a desired stiffness, damping and mass on the end effector. Therefore, it can be concluded, that the control algorithm is working properly.

The range of desired dynamics projected on the end effector of the test setup, the Munin, is obtained by a manual iterative process. The range of the possible maximum damping mass ratio $M_{\mathrm{d}}^{-1}K_{\mathrm{D_d}}$ is $250\frac{1}{\mathrm{s}}$ in p_x and p_y and $156.5\frac{1}{\mathrm{rad}\cdot\mathrm{s}}$ in p_{θ_z}. The maximal stiffness mass ratio $M_{\mathrm{d}}^{-1}K_{\mathrm{P_d}}$ is $15790\frac{1}{\mathrm{s}^2}$ for p_x and p_y and $6667.725\frac{1}{\mathrm{rad}\cdot\mathrm{s}^2}$ for p_{θ_z}. The desired mass can be increased from the average of the real mass, 0.2 kg. A decrease of the mass can be implemented down to 0.1 kg, but significant damping has to be added to keep the system stable.

Within the given ranges it is shown, that an admittance controller can be implemented on a parallel haptic master device without a force sensor. This can be implemented on the master device of a telemanipulation system, and on other devices, where humans interact physically with robots. Because no force sensors will have to be used, good performance can be reached with a significant reduction of the costs.

Appendix A

Munin inertia matrix

In this appendix, the inertia matrix for the Munin is represented graphically. The value of the matrix entries of the inertia matrix is shown on the z-axis for all p_x and p_y on respectively the x- and y-axis. This is shown for three cases of p_{θ_z}: $\begin{Bmatrix} -0.8 & 0 & 0.8 \end{Bmatrix}$. The nine plots for each p_{θ_z} represent the values of the inertia matrix in the following form:

$$M(p) = \begin{bmatrix} M_{\theta\theta} & M_{\theta x} & M_{\theta y} \\ M_{x\theta} & M_{xx} & M_{xy} \\ M_{y\theta} & M_{yx} & M_{yy} \end{bmatrix}. \tag{A-1}$$

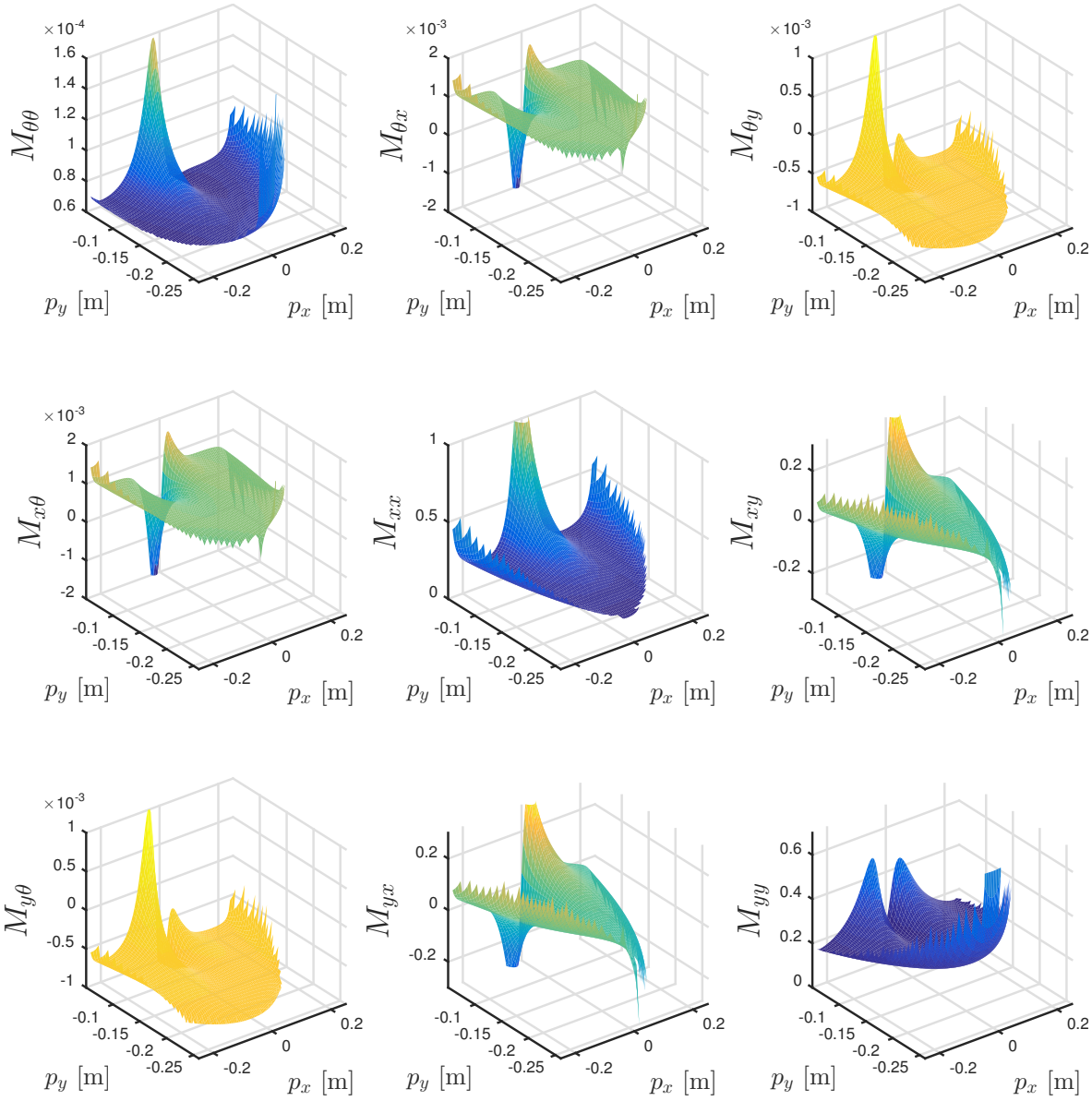

Figure A-1: Inertia matrix for $p_{\theta_z} = -0.8$

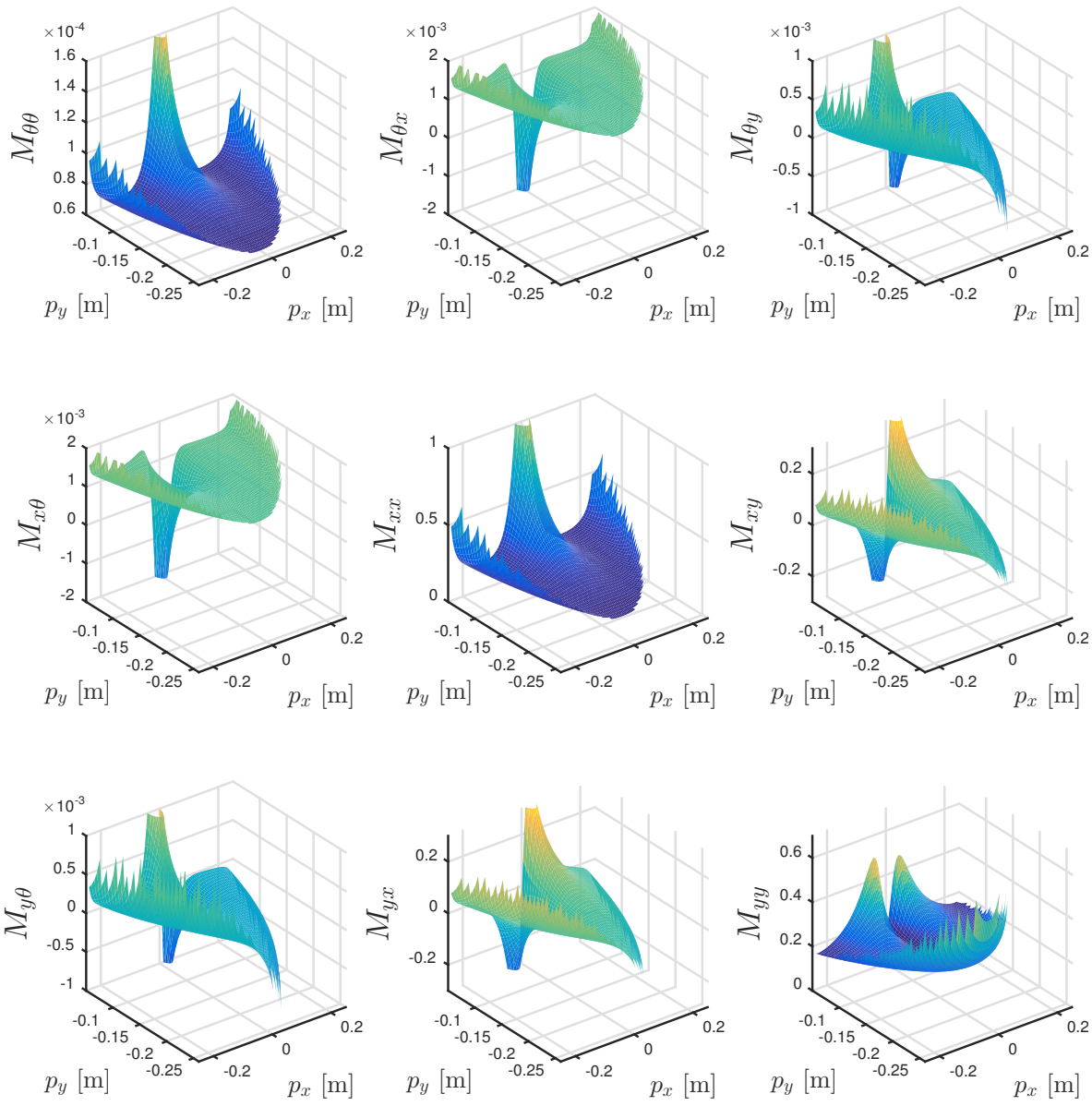

Figure A-2: Inertia matrix for $p_{\theta_z} = 0$

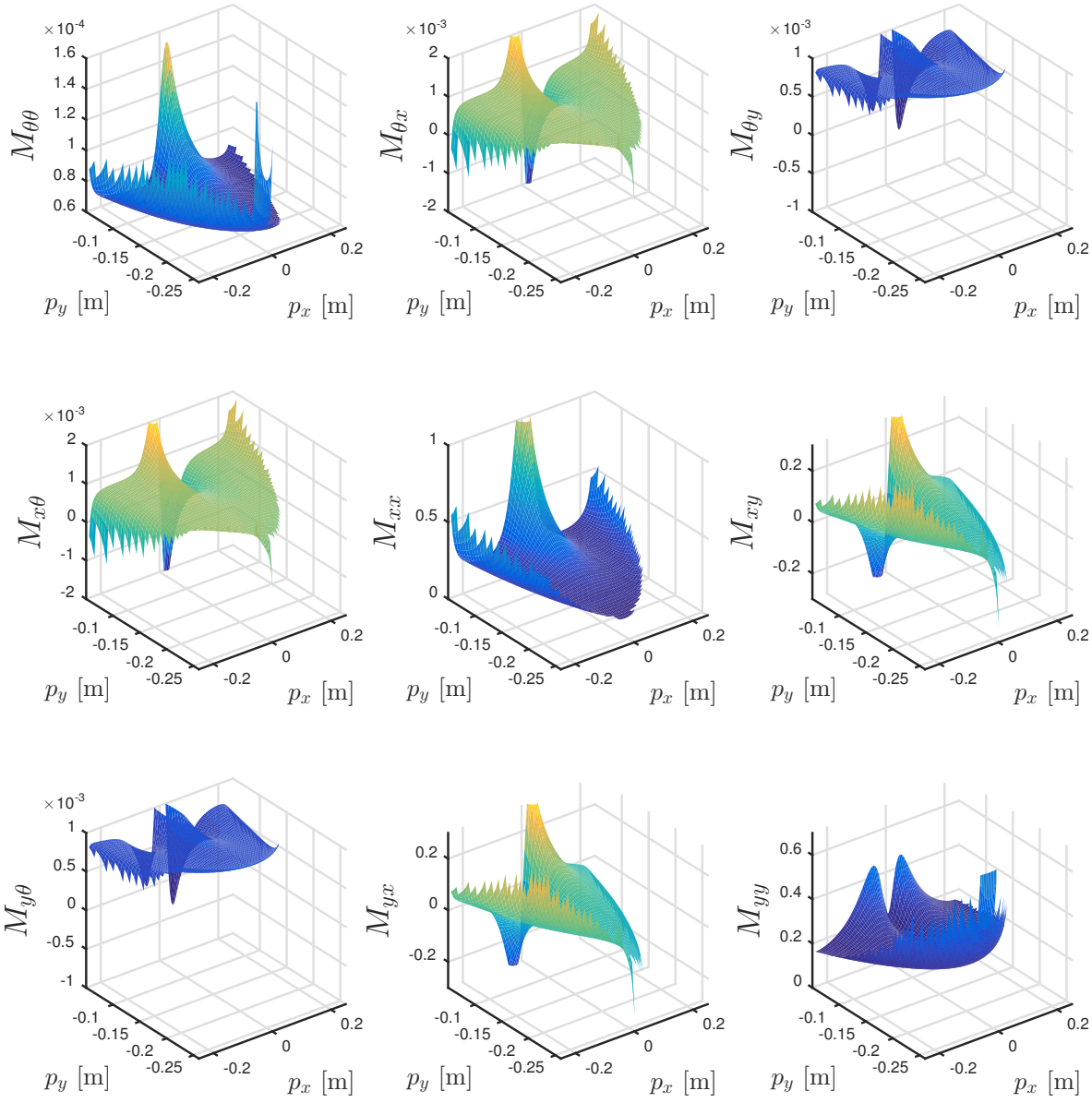

Figure A-3: Inertia matrix for $p_{\theta_z} = 0.8$

Appendix B

Step responses for the range of $K_{\mathbf{P_d}}$ and $K_{\mathbf{D_d}}$

To find the range of possible projected stifnesses $K_{\mathrm{P_d}}$ and dampings $K_{\mathrm{D_d}}$ values for a diagonal desired mass matrix, close to the non-linear and non-diagonal real mass matrix,

$$M_{\mathrm{d}} = \begin{bmatrix} 6.389{\cdot}10^{-5} & 0 & 0 \\ 0 & 0.2 & 0 \\ 0 & 0 & 0.2 \end{bmatrix}, \tag{B-1}$$

steps on the reference in all direction are performed to test the stability and capability to overcome the small static friction. Steps for the extreme and in-between values are shown in this appendix. The resulting response is plotted in position (y-axis) versus time (x-axis) and in velocity (y-axis) versus the position (x-axis). The results for a damping ratio ζ of 1, 0.5 and 0.2 is shown for

$$K_{\mathrm{P_d}} = \begin{bmatrix} 0.4 & 0 & 0 \\ 0 & 3158 & 0 \\ 0 & 0 & 3158 \end{bmatrix} \text{ (figure B-1)}, \tag{B-2}$$

$$K_{\mathrm{P_d}} = \begin{bmatrix} 0.085 & 0 & 0 \\ 0 & 639.55 & 0 \\ 0 & 0 & 639.55 \end{bmatrix} \text{ (figure B-2), and} \tag{B-3}$$

$$K_{\mathrm{P_d}} = \begin{bmatrix} 0.0043 & 0 & 0 \\ 0 & 31.58 & 0 \\ 0 & 0 & 31.58 \end{bmatrix} \text{ (figure B-3).} \tag{B-4}$$

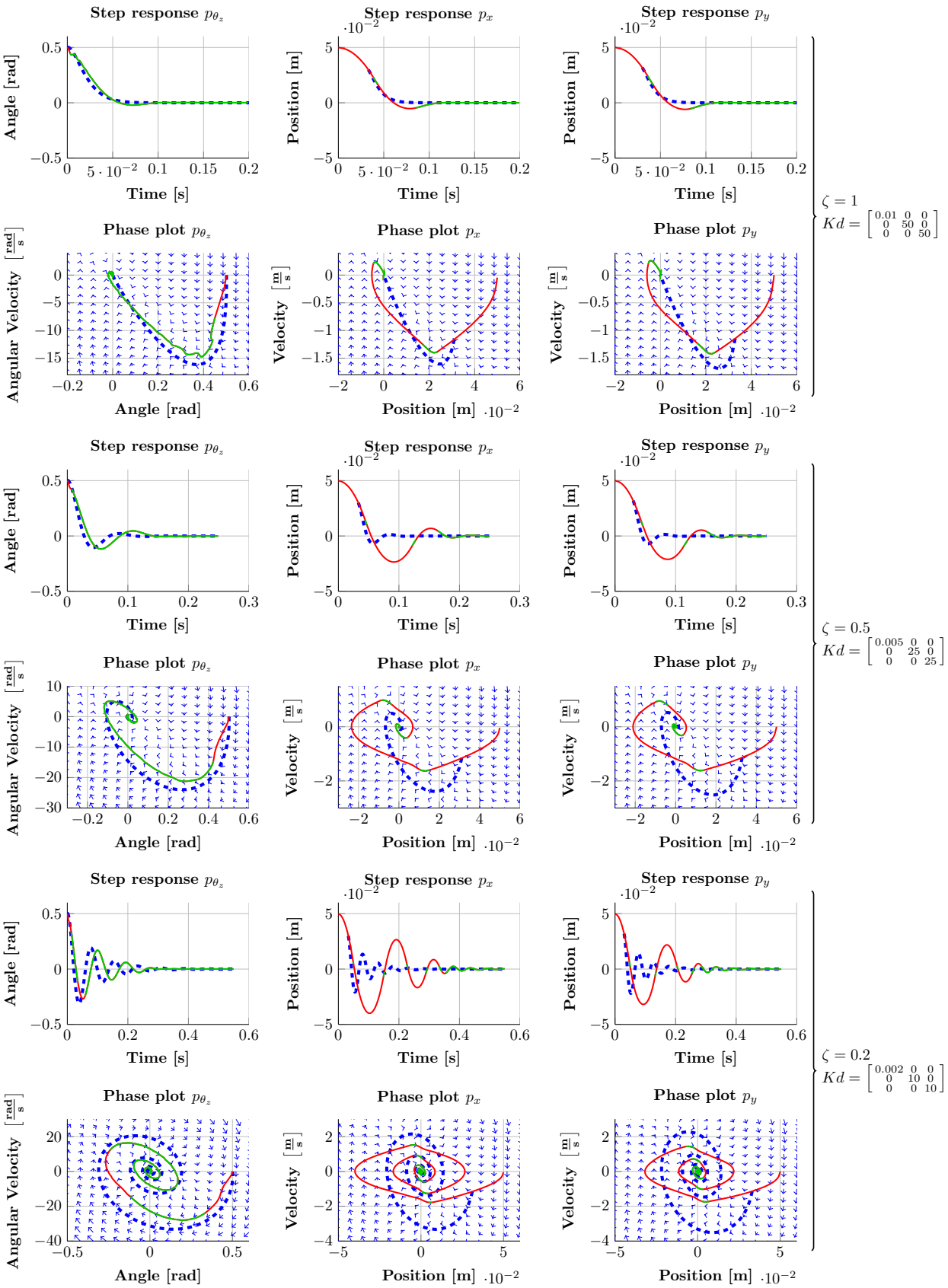

Figure B-1: Response for steps on the reference of p_{θ_z} (left), p_x (middle), and p_y (right) for Kp= $\begin{bmatrix} 0.4 & 0 & 0 \\ 0 & 3158 & 0 \\ 0 & 0 & 3158 \end{bmatrix}$ and three different Kd as described on the right side of the graphs. The expected result is shown with the blue vector field and dotted line. The measure response is shown in green and red. The red parts indicate that one of the motors was saturated.

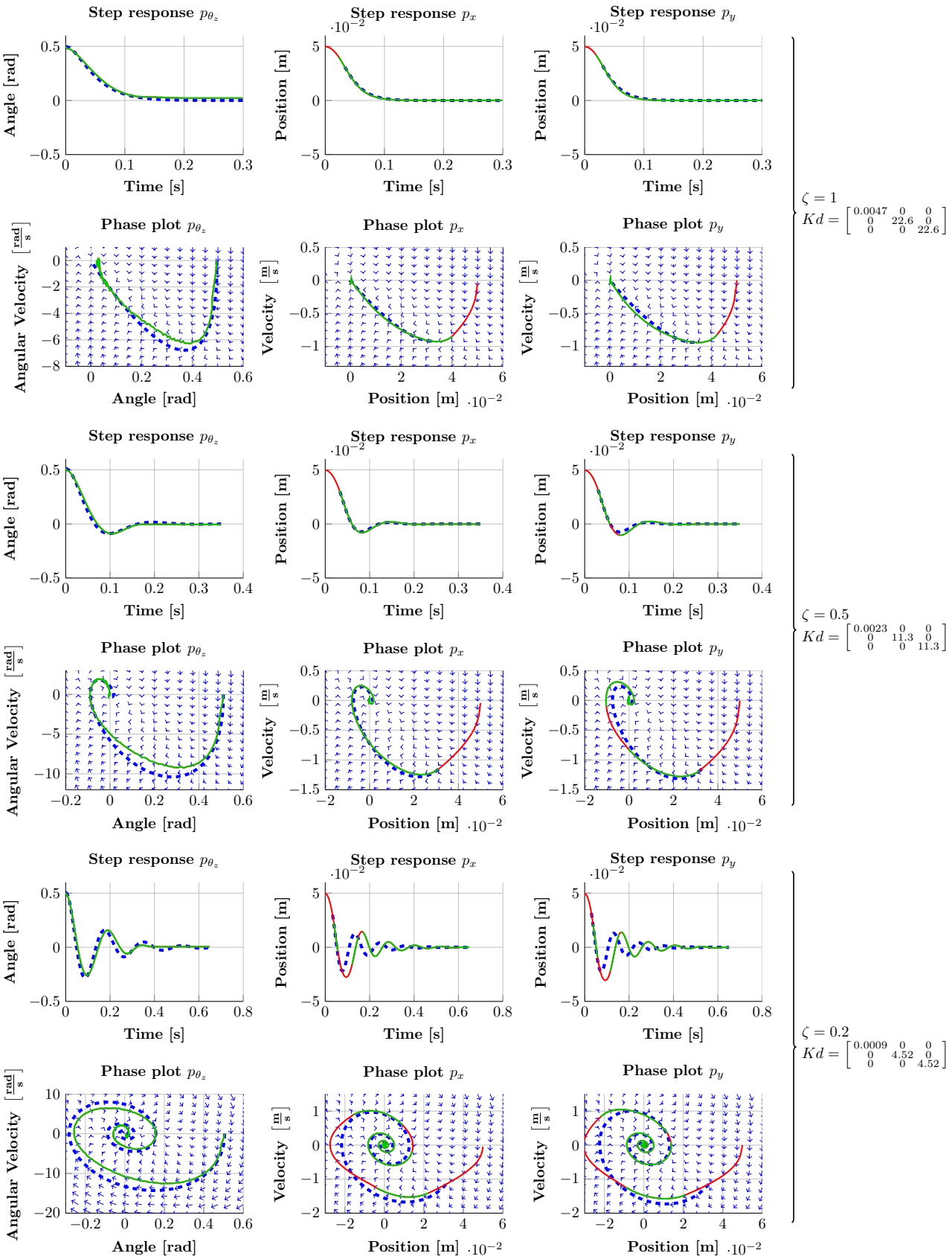

Figure B-2: Response for steps on the reference of p_{θ_z} (left), p_x (middle), and p_y (right) for Kp= $\begin{bmatrix} 0.085 & 0 & 0 \\ 0 & 639.55 & 0 \\ 0 & 0 & 639.55 \end{bmatrix}$ and three different Kd as described on the right side of the graphs. The expected result is shown with the blue vector field and dotted line. The measure response is shown in green and red. The red parts indicate that one of the motors was saturated.

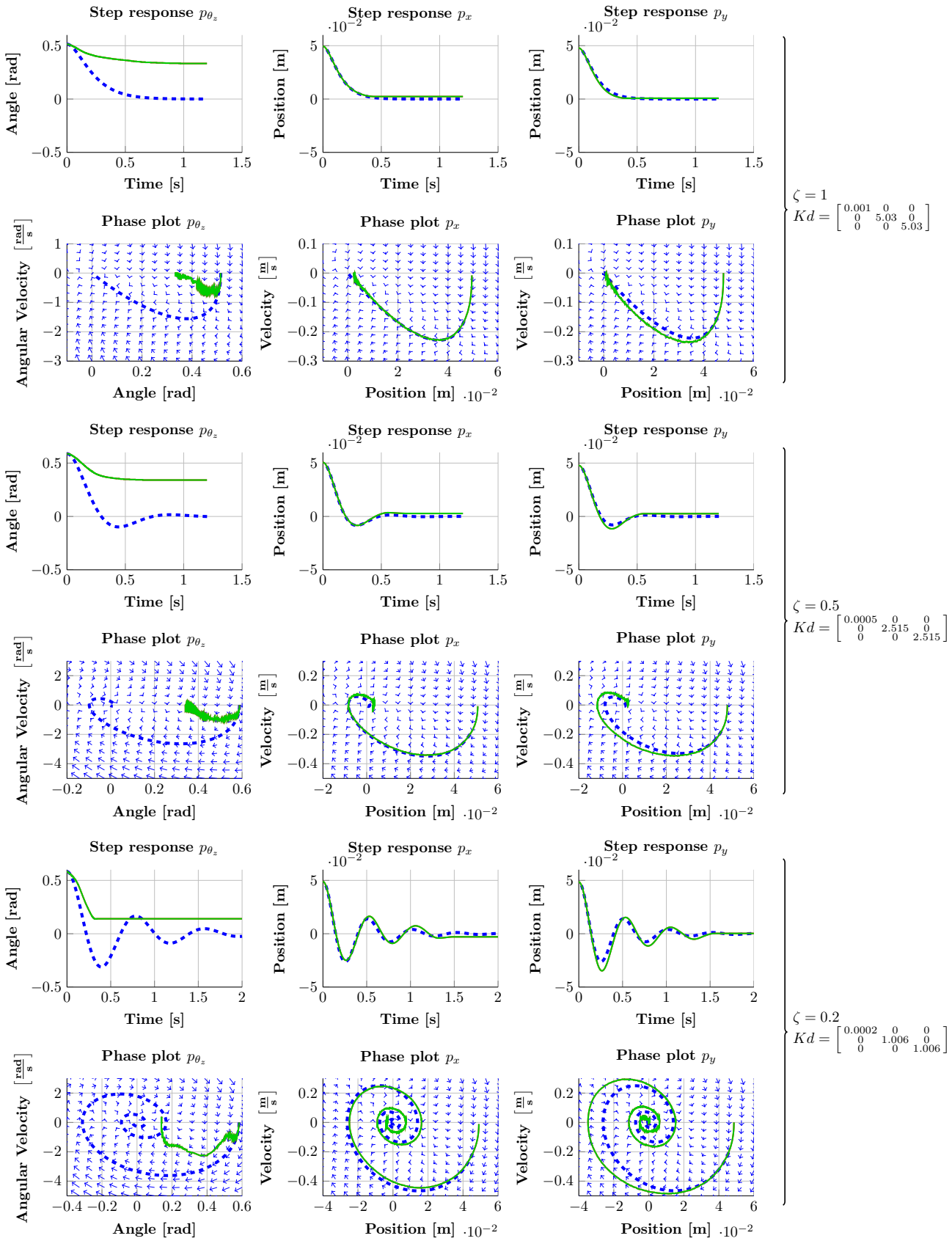

Figure B-3: Response for steps on the reference of p_{θ_z} (left), p_x (middle), and p_y (right) for Kp= $\begin{bmatrix} 0.0043 & 0 & 0 \\ 0 & 31.58 & 0 \\ 0 & 0 & 31.58 \end{bmatrix}$ and three different Kd as described on the right side of the graphs. The expected result is shown with the blue vector field and dotted line. The measure response is shown in green and red. The red parts indicate that one of the motors was saturated.

Bibliography

[1] P. Estevez, S. Khan, P. Lambert, M. Porta, and I. Polat, "A Haptic Tele-operated System for Microassembly," pp. 13–20.

[2] S. Grange, F. Conti, P. Helmer, P. Rouiller, and C. Baur, "The Delta Haptic Device as a nanomanipulator," vol. 4568, pp. 100–111, 2001.

[3] D. Navarro-Alarcon, "Stable force/position control of a robotic endoscope holder for constrained tasks in nasal surgery," *2011 9th World Congress on Intelligent Control and Automation*, pp. 1195–1200, jun 2011.

[4] D. a. Lawrence, "Stability and transparency in bilateral teleoperation," *IEEE Transactions on Robotics and Automation*, vol. 9, no. 5, pp. 624–637, 1993.

[5] F. Avanzini and P. Crosato, "Integrating physically based sound models in a multimodal rendering architecture," *Computer Animation and Virtual Worlds*, vol. 17, no. 3-4, pp. 411–419, 2006.

[6] V. Hayward and K. Maclean, "Do it yourself haptics: part I," *IEEE Robotics & Automation Magazine*, vol. 14, pp. 88–104, dec 2007.

[7] a. M. Okamura, J. T. Dennerlein, and R. D. Howe, "Vibration feedback models for virtual environments," *Robotics and Automation, 1998. Proceedings. 1998 IEEE International Conference on*, vol. 1, no. May, pp. 674–679 vol.1, 1998.

[8] M. I. C. Dede and S. Tosunoglu, "Parallel position/force controller for teleoperation systems," 2007.

[9] R. Adams and B. Hannaford, "Stable haptic interaction with virtual environments," *IEEE Transactions on Robotics and Automation*, vol. 15, pp. 465–474, jun 1999.

[10] R. Adams and B. Hannaford, "Control law design for haptic interfaces to virtual reality," *IEEE Transactions on Control Systems Technology*, vol. 10, no. 1, pp. 3–13, 2002.

[11] S. P. Buerger and N. Hogan, "Relaxing passivity for human-robot interaction," *IEEE International Conference on Intelligent Robots and Systems*, pp. 4570–4575, 2006.

[12] J.-P. Merlet, *Parallel robots*, vol. 74. Springer, 2001.

[13] R. M. Murray, Z. Li, and S. S. Sastry, *A Mathematical Introduction to Robotic Manipulation*. CRC Press, 1994.

[14] S. A. Joshi and L.-W. Tsai, "Jacobian Analysis of Limited-DOF Parallel Manipulators," *Journal of Mechanical Design*, vol. 124, no. 2, p. 254, 2002.

[15] T. Huang, H. T. Liu, and D. G. Chetwynd, "Generalized Jacobian analysis of lower mobility manipulators," *Mechanism and Machine Theory*, vol. 46, pp. 831–844, jun 2011.

[16] M. G. Mohamed and J. Duffy, "A Direct Determination of the Instantaneous Kinematics of Fully Parallel Robot Manipulators," *Journal of Mechanisms Transmissions and Automation in Design*, vol. 107, no. 2, p. 226, 1985.

[17] S. Briot and M. Gautier, "Global identification of joint drive gains and dynamic parameters of parallel robots," *Multibody System Dynamics*, dec 2013.

[18] F. Aghili and A. Member, "A Unified Approach for Inverse and Direct Dynamics of Constrained Multibody Systems Based on Linear Projection Operator : Applications to Control and Simulation," vol. 21, no. 5, pp. 834–849, 2005.

[19] W. Khalil and O. Ibrahim, "General Solution for the Dynamic Modeling of Parallel Robots," *Journal of Intelligent and Robotic Systems*, vol. 49, pp. 19–37, 2007.

[20] J. Wang and C. M. Gosselin, "A New Approach for the Dynamic Analysis of Parallel Manipulators," pp. 317–334, 1998.

[21] J. Y. S. Luh, R. P. C. Paul, and M. W. Walker, "Resolved-Acceleration Control of Mechanical Manipulators," *IEEE Transactions on Automatic Control*, vol. 25, no. 3, pp. 468–474, 1980.

[22] D. R. Uecker, S. Barbara, and T. Kokkinis, "Experimental Evaluation of Real-Time Model-Based Control of a 3-DOF Closed-Chain Direct-Drive Mechanism," no. April, pp. 1861–1866, 1991.

[23] S. Bellakehal, N. Andreff, Y. Mezouar, and M. Tadjine, "Force/position control of parallel robots using exteroceptive pose measurements," *Meccanica*, vol. 46, pp. 195–205, jan 2011.

[24] M. Callegari, M.-C. Palpacelli, and M. Principi, "Dynamics modelling and control of the 3-RCC translational platform," *Mechatronics*, vol. 16, pp. 589–605, dec 2006.

[25] Q. Daun, B. Daun, and X. Daun, "Dynamics modelling and hybrid control of the 6-UPS platform," *2010 IEEE International Conference on Mechatronics and Automation*, pp. 434–439, aug 2010.

[26] P. Taylor, O. Korkmaz, and S. K. Ider, "Hybrid force and motion control of flexible joint parallel manipulators using inverse dynamics approach," *Advanced Robotics*, no. August, pp. 37–41, 2014.

[27] S. Tadokoro, "Control of parallel mechanisms," *Advanced Robotics*, vol. 8, pp. 559–571, jan 1993.

[28] J. J. Abbott and A. M. Okamura, "Pseudo-admittance Bilateral Telemanipulation with Guidance Virtual Fixtures," *Haptic Interfaces for Virtual Environment and Teleoperator Systems, 2006 14th Symposium on*, pp. 169–175, 2006.

[29] C. L. Clover, "A control-system architecture for robots used to simulate dynamic force and moment interaction between humans and virtual objects," *IEEE transactions on systems, man and cybernetics. Part C, Applications and reviews*, vol. 29, no. 4, pp. 481–493, 1999.

[30] R. van der Linde and P. Lammertse, "HapticMaster - a generic force controlled robot for human interaction," *Industrial Robot: An International Journal*, vol. 30, no. 6, pp. 515–524, 2003.

[31] P. Hacksel and S. Salcudean, "Estimation of environment forces and rigid-body velocities using observers," *Proceedings of the 1994 IEEE International Conference on Robotics and Automation*, pp. 931–936, 1994.

[32] A. Alcocera, A. Robertssona, A. Valerac, and R. Johanssona, "Force estimation and control in robot manipulators," in *Robot Control 2003 (SYROCO'03): A Proceedings Volume from the 7th IFAC Symposium, Wrocław, Poland, 1-3 September 2003*, vol. 1, p. 55, International Federation of Automatic Control, 2004.

[33] H. Boessenkool, D. a. Abbink, C. J. Heemskerk, F. C. van der Helm, and J. G. Wildenbeest, "A Task-Specific Analysis of the Benefit of Haptic Shared Control During Tele-Manipulation," *IEEE Transactions on Haptics*, pp. 1–1, 2012.

[34] C. Passenberg, A. Peer, and M. Buss, "Model-Mediated Teleoperation for Multi-Operator Multi-Robot Systems," pp. 4263–4268, 2010.

List of Symbols

Table B-1: List of symbols

$\mathsf{J}_{r,t}$	The t^{th} joint of the r^{th} leg of the device. For a general r and t also written as J.
$\mathsf{L}_{r,s}$	The s^{th} link of the r^{th} leg of the device. For a general r and s also written as L.
Ψ_l	Coordinate system l.
α_u^l	Point u in Ψ_l.
H_l^m	Homogeneous transformation matrix maps a point in Ψ_l to Ψ_m.
o_l^m	A point in the origin of Ψ_l expressed in Ψ_m.
$T_l^{k,m}$	The twist of Ψ_l with respect to Ψ_m expressed in Ψ_k.
$\hat{T}_l^{k,m}$	The unit twist of Ψ_l with respect to Ψ_m expressed in Ψ_k.
W_l^m	A wrench between Ψ_l and Ψ_m.
$Ad_{H_n^k}$	The adjoint matrix of H_n^k.
$q_{r,t}$	The joint coordinate of the t^{th} joint of the r^{th} leg. Also q is used for all joint coordinates and q_{a} for the actuated joint coordinates.
p	End effector / workspace coordinates.
G	Inverse kinematics function
D	Forward kinematics function
J	Jacobian matrix. Maps velocities between workspace coordinates p en joint coordinates q_{a} when there are no subscripts. With subscripts, the velocity mapping is explained in the text.
$\tau_{q_{\text{a}}}$	Control torques.
$\tau_{q_{\text{a}},\text{fr}}(\dot{p})$	Friction torques.
$W_{\mathsf{P}\,\text{c}}^{\mathsf{B}}$	Control torques $\tau_{q_{\text{a}}}$ written as wrench at the end effector.
$W_{\mathsf{P}\,\text{ext}}^{\mathsf{B}}$	External wrench at the end effector (applied by the operator).
$M(p)$	Mass / inertia matrix
$C(p,\dot{p})$	Coriolis tensor
$K(p)$	Stiffness and gravitational forces
M_{d}	Desired mass / inertia matrix
$K_{\text{D}_{\text{d}}}$	Desired damping matrix
$K_{\text{P}_{\text{d}}}$	Desired stiffness matrix
e_p	Position error: Difference between desired and real end effector position
$\dot{e}_p$	Velocity error: Difference between desired and real end effector velocity
$e_{\hat{p}}$	Observer error: Difference between measured and observer position
L	Observer gain.
B	Filter for velocity component in force estimator.
k_{ext}	Spring constant of external springs, used for validation.
$\hat{}$ (hat)	Observer estimate (or unit twist in $\hat{T}_l^{k,m}$).
$\tilde{}$ (tilde)	Modelled version (or tilde matrix of a vector).